A Novel Hybrid Machine Tool Integrating a Symmetrical Redundantly Actuated Parallel Mechanism: Design, Kinematics, Prototype and Experiment

Hanliang Fang[a], Tengfei Tang[a], Zhen He[a], Yuanchang Liu[b], Jun Zhang[a, c, *]

a. School of Mechanical Engineering and Automation, Fuzhou University, Fujian 350116, China
b. Department of Mechanical Engineering, University College London, Torrington Place, London WC1E 7JE, UK
c. The State Key Laboratory of Mechanical Transmissions, Chongqing University, Chongqing 400044, China

Abstract: Hybrid machine tools are suitable for machining structural components with complex geometries due to their merits of flexible posture adjustment and quick dynamic response. This paper proposes a novel hybrid machine tool with 5-axis machining capability by integrating a newly invented redundantly actuated parallel mechanism (RAPM). For this purpose, a screw theory based type synthesis methodology is proposed to synthesize a RAPM with a topology of 2PRU-(2PRU)R. The synthesized RAPM is conceptually designed as a spindle head, which is characterized by symmetrical limb arrangement and usage of only PRU-type kinematic chains. The spindle head is further integrated with a two-sliding gantry to construct a novel 5-axis hybrid machine tool. The kinematic performances of position and singularity of the proposed hybrid machine tool are analyzed. After then, a laboratory prototype of the hybrid machine tool is engineered and an open-architecture numerical control system is developed to perform 5-axis machining tasks. The large orientation capacity and 5-axis machining capability of the hybrid machine tool are verified by some motion experiments and machining tests.

Keywords: hybrid machine tool; redundantly actuated; parallel mechanism; 5-axis machining

1. Introduction

There is an emerging demand for high-efficiency machining of structural components with complex geometries in modern manufacturing industries where compound angle machining and high material removal rate are often required [1-4]. Such a demand brings considerable challenges to the traditional stack-up machine tools [5, 6]. To deal with these challenges, concept of hybrid machine tools has been proposed as an alternative solution due to their conceptual advantages of flexible posture adjustment and quick dynamic response [7-10]. After decades of efforts from both academic and industrial communities, hybrid machine tools have gradually found their promising applications in various manufacturing fields such as aeronautics, astronautics, vehicles and shipping [5, 11, 12].

As evidenced by the commercial success of Ecospeed [13], Tricept [14] and Exechon [15], a typical hybrid machine tool with 5-axis machining capability usually consists of a one translation and two rotations (1T2R) parallel mechanism module functioned as orientation adjustment unit and a 2-DOF (DOF: degree of freedom) serial mechanism module functioned as position adjustment unit or vice versa. For example, Ecospeed [13] integrates a 1T2R parallel module named Sprint Z3 head with two orthogonal sliding gantries. Exechon [16] and Tricept [17] are constructed by connecting a 2-DOF wrist joint to a 1T2R parallel manipulator.

It should be pointed out that parallel mechanism functional modules of hybrid machine tools are versatile and less developed, when compared with the well-developed serial mechanism functional module. Thus, the critical issue, i.e. how to design a desirable parallel mechanism functional module through solid theoretical derivation, should be conducted in the early design stage of constructing a hybrid machine tool. For this reason, many scholars have devoted their time and effort to type synthesis of parallel manipulators [18-24]. The parallel mechanism can be roughly classified into two categories: non-redundantly actuated parallel mechanism and redundantly actuated parallel mechanism (RAPM) according to the relationship between its DOFs and the number of actuators. Previous studies [25-27] indicate that a RAPM module may

*Corresponding author: Jun Zhang
E-mail address: zhang_jun@fzu.edu.cn

possess higher stability, larger dexterous workspace and fewer singular postures than its counterpart of non-redundantly actuated parallel mechanism due to the introduction of redundancy. In view of these merits, a number of 1T2R RAPM were proposed and applied for constructing hybrid machine tools [28-30].

From the perspective of mechanism, a 1T2R RAPM can be constructed through the followings three traditional manners: (1) replacing one or more passive joints with active joints in an original parallel mechanism [30]; (2) adding a full-mobility active kinematic chain into an original parallel mechanism [29, 31]; (3) introducing a lower-mobility active kinematic chain to an original parallel mechanism [32, 33]. By adopting above three manners, a series of 1T2R RAPMs have been proposed in the past years [34-36]. However, it needs to point out that these 1T2R RAPMs may still have one or more followings critical drawbacks:

(1) Strong anisotropy of performance distribution within the workspace in terms of parasitic motion, orientation, dexterity, motion/force transmissibility, rigidity and dynamics [32, 34]. The reason may lie in the utilization of different types of kinematic chains and the non-intersection of two virtual rotational axes. To improve the performance isotropy of a RAPM, it is suggested to adopt identical type of kinematic chains to construct a RAPM with symmetrical structures.

(2) Excessive over-constraints may be introduced into a RAPM. It has been proven that internal forces will be introduced into an over-constraint parallel manipulator, when their real structural parameters are not equal to their ideal values [37-39]. This makes the RAPM very sensitive to geometric errors as well as assembling errors. In other words, a tiny deviation from the ideal kinematic dimension will arouse significant internal loads and even cause mechanism jamming. This, in turn, brings considerable challenges to the tolerance design, manufacturing and assembling of the RAPM. From the point of reducing error sensitivity, it is recommended to introduce less over-constrains into the original system and construct a symmetrical constraint structure in which only one over-constraint is generated in each individual direction.

(3) Spherical joint caused performance deficiency. There are two typical types of spherical joint used in parallel manipulator: 1. a spherical joint is realized by a concave spherical surface and a concave spherical surface; 2. a spherical joint is realized by three revolute joints with three non-coplanar axes intersecting at a point. For the first type, it can be predicted that it is very difficult to satisfy the strict requirement of small contact clearance between the concave spherical surface and the concave spherical surface. In other word, this may be a very challenging work to produce such a spherical joint with high precision, high quality and high wear resistance [40-42]. For the second type, it possesses more components and single-DOF joint than a revolute joint or a universal joint. This may introduce more assembly and manufacturing error sources, limit the geometrical dimension of single component for large joint workspace, and even decrease the payload to weight ratio. Thus, it is more difficult to guarantee the tolerance and the stiffness of spherical joint under similar manufacturing level when compared with revolute joint or universal joint. As a result, a RAPM containing spherical joint may suffer from problems of low accuracy and small payload to weight ratio in practical applications. To avoid the deficiency generated by a spherical joint, it is preferred to adopt a lower-mobility kinematic chain without spherical joint to construct a RAPM.

Bearing with the above thoughts, this paper invents a 1T2R RAPM which only consists of PRU-type lower-mobility kinematic chains with symmetrical structural arrangements. Herein, 'P', 'R' and 'U' represent a prismatic joint, a revolute joint and a universal joint, respectively. With the newly invented RAPM, a hybrid machine tool with 5-axis motion capabilities will be constructed. Before it can be used as a machining solution, some fundamental investigations need to be carried out in the early engineering design stages. To be specific, the conceptual design and the kinematic properties of the RAPM module as well as the overall hybrid machine tool should be conducted to provide necessary information for workspace selection, trajectory planning and motion controlling. In addition, to verify the feasibility of the proposition, a laboratory prototype with an open-architecture control system will be engineered and some motion experiments and machining tests will be carried out. It is believed that the present study will enrich the type synthesis theory of parallel mechanisms and expand the design scope of hybrid machine tools. Also, it is expected to provide a promising machining solution for structural components with complex geometries.

The remainder of this paper is organized as follows. In Section 2, a type synthesis for 1T2R RAPMs with symmetrical PRU-type kinematic chains is conducted followed by a conceptual design for the parallel module of spindle head. Section 3 focuses on the kinematics of the RAPM module as well as the overall hybrid machine tool including the inverse/forward position analysis, the velocity solution and the singularity analysis. Section 4 proposes a horizontal-type hybrid machine tool and carries out its position analysis and orientation workspace prediction. In Section 5, a laboratory prototype is fabricated and a self-developed control system is presented. With the developed prototype, a set of motion experiments and machining tests are performed to verify the feasibility of the proposed 5-axis hybrid machine tool. Finally, some conclusions are drawn to close the paper.

2. Type synthesis of 1T2R RAPM

In this section, a new family of 1T2R RAPM with PRU-type kinematic chain is developed. Herein, a PRU-type kinematic chain refers to a kinematic chain only consists of a prismatic joint, a revolute joint and a universal joint.

2.1. Over-constraint characteristics of two PRU-type kinematic chains

For the sake of generality, Fig. 1 illustrates the diagram of the i^{th} PRU-type kinematic chain of a RAPM in a general coordinate system O_g-$x_g y_g z_g$.

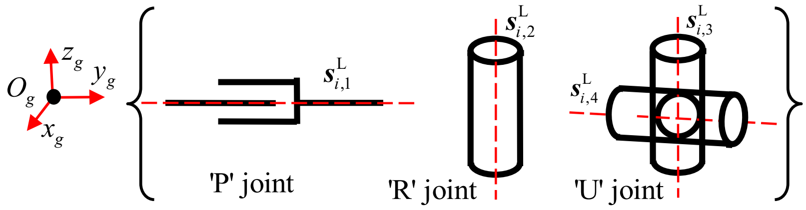

Fig. 1 The diagram of the i^{th} PRU-type kinematic chain

As shown in Fig. 1, $\boldsymbol{s}^{L}_{i,j}$ (j= 1-2) denotes a unit vector along the j^{th} single-DOF joint axis of the i^{th} PRU-type kinematic chain. The geometrical constraints of an individual PRU-type chain can be described as the follows.

1) $\boldsymbol{s}^{L}_{i,2}$ and $\boldsymbol{s}^{L}_{i,3}$ are parallel to each other.

2) $\boldsymbol{s}^{L}_{i,1}$ and $\boldsymbol{s}^{L}_{i,4}$ are perpendicular to $\boldsymbol{s}^{L}_{i,2}$ simultaneously.

Letting $\$_{i,j}$ denotes a unit screw of the j^{th} single-DOF joint of the i^{th} PRU-type kinematic chain, the twist system [25] of a PRU-type kinematic chain can be given by

$$\begin{cases} \$_{i,1} = [\mathbf{0}; \boldsymbol{s}^{L}_{i,1}] \\ \$_{i,2} = [\boldsymbol{s}^{L}_{i,2}; \boldsymbol{r}_{Ri} \times \boldsymbol{s}^{L}_{i,2}] \\ \$_{i,3} = [\boldsymbol{s}^{L}_{i,3}; \boldsymbol{r}_{Ui} \times \boldsymbol{s}^{L}_{i,3}] \\ \$_{i,4} = [\boldsymbol{s}^{L}_{i,4}; \boldsymbol{r}_{Ui} \times \boldsymbol{s}^{L}_{i,4}] \end{cases} \tag{1}$$

where $\boldsymbol{r}_{Ri}$ and $\boldsymbol{r}_{Ui}$ denotes the position vectors of the geometric centre of revolute joint and universal joint measured in the frame of O_g-$x_g y_g z_g$, respectively.

By using the reciprocal screw theory [39, 43, 44], one may obtain the wrench system of a PRU-type chain as

$$\begin{cases} \hat{\$}_{i,1} = [\mathbf{0}; \boldsymbol{s}_{i,3}^{\mathrm{L}} \times \boldsymbol{s}_{i,4}^{\mathrm{L}}] \\ \hat{\$}_{i,2} = [\boldsymbol{s}_{i,2}^{\mathrm{L}}; \boldsymbol{r}_{s_{i,4}} \times \boldsymbol{s}_{i,2}^{\mathrm{L}}] \end{cases} \tag{2}$$

where $\hat{\$}_{i,1}$ represents a constraint moment constraining the rotation about the axis perpendicular to $\boldsymbol{s}_{i,3}^{\mathrm{L}}$ and $\boldsymbol{s}_{i,4}^{\mathrm{L}}$ simultaneously; $\hat{\$}_{i,2}$ denotes a constraint force parallel to $\boldsymbol{s}_{i,2}^{\mathrm{L}}$ and passing through any point on the vector of $\boldsymbol{s}_{i,4}^{\mathrm{L}}$; $\boldsymbol{r}_{s_{i,4}}$ is a position vector of any point on the vector of $\boldsymbol{s}_{i,4}^{\mathrm{L}}$.

Based on the above derivation, it can be found that there are three cases in which an over-constraint is produced between any two PRU-type kinematic chains as shown in Fig. 2. The details of three cases are described as follows.

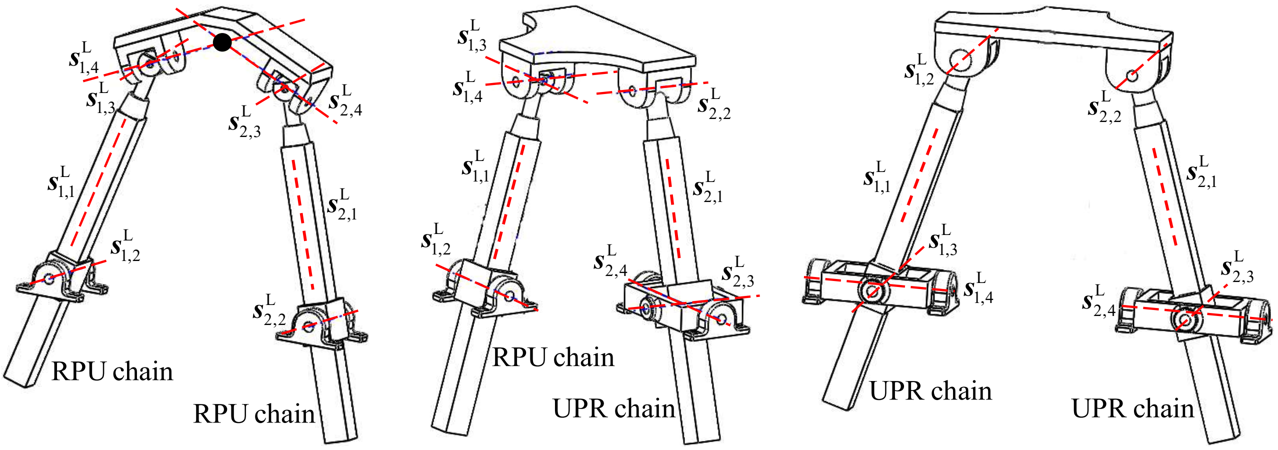

(a) 2RPU (b) 1UPR-1RPU (c) 2UPR

Fig. 2 Structural scheme of three types of chain system with equivalent constraint

For case 1: the two constraint forces are equivalent constraints but the two constraint moments are not equivalent.

For such a case, there exists

$$\begin{cases} [\boldsymbol{s}_{1,2}^{\mathrm{L}}; \boldsymbol{r}_{s_{1,4}} \times \boldsymbol{s}_{1,2}^{\mathrm{L}}] = [\boldsymbol{s}_{2,2}^{\mathrm{L}}; \boldsymbol{r}_{s_{2,4}} \times \boldsymbol{s}_{2,2}^{\mathrm{L}}] \\ [\mathbf{0}; \boldsymbol{s}_{1,3}^{\mathrm{L}} \times \boldsymbol{s}_{1,4}^{\mathrm{L}}] \neq [\mathbf{0}; \boldsymbol{s}_{2,3}^{\mathrm{L}} \times \boldsymbol{s}_{2,4}^{\mathrm{L}}] \end{cases} \tag{3}$$

Eq. (3) can be rewritten as the following

$$\begin{cases} \boldsymbol{s}_{1,2}^{\mathrm{L}} = \boldsymbol{s}_{2,2}^{\mathrm{L}} \\ \boldsymbol{r}_{s_{1,4}} \times \boldsymbol{s}_{1,2}^{\mathrm{L}} = \boldsymbol{r}_{s_{2,4}} \times \boldsymbol{s}_{2,2}^{\mathrm{L}} \\ \boldsymbol{s}_{1,3}^{\mathrm{L}} \times \boldsymbol{s}_{1,4}^{\mathrm{L}} \neq \boldsymbol{s}_{2,3}^{\mathrm{L}} \times \boldsymbol{s}_{2,4}^{\mathrm{L}} \end{cases} \tag{4}$$

It can be judged from Eq. (4) that two PRU-type kinematic chains will have only one over-constraint force when satisfying: (1) $\boldsymbol{s}_{1,4}^{\mathrm{L}}$ and $\boldsymbol{s}_{2,4}^{\mathrm{L}}$ are intersecting but not collinear; (2) $\boldsymbol{s}_{1,2}^{\mathrm{L}}$ and $\boldsymbol{s}_{2,2}^{\mathrm{L}}$ are parallel to each other. This circumstance can be graphically illustrated by a 2RPU combination as shown in Fig. 2 (a).

For case 2: the two constraint moments are equivalent constraints but the two constraint forces are not equivalent. For such a case, there exists

$$\begin{cases} [\mathbf{0}; \boldsymbol{s}_{1,3}^{\mathrm{L}} \times \boldsymbol{s}_{1,4}^{\mathrm{L}}] = [\mathbf{0}; \boldsymbol{s}_{2,3}^{\mathrm{L}} \times \boldsymbol{s}_{2,4}^{\mathrm{L}}] \\ [\boldsymbol{s}_{1,2}^{\mathrm{L}}; \boldsymbol{r}_{s_{1,4}} \times \boldsymbol{s}_{1,2}^{\mathrm{L}}] \neq [\boldsymbol{s}_{2,2}^{\mathrm{L}}; \boldsymbol{r}_{s_{2,4}} \times \boldsymbol{s}_{2,2}^{\mathrm{L}}] \end{cases} \tag{5}$$

Eq. (5) can be rewritten as the following

$$\begin{cases} \boldsymbol{s}_{1,3}^{\mathrm{L}} \times \boldsymbol{s}_{1,4}^{\mathrm{L}} = \boldsymbol{s}_{2,3}^{\mathrm{L}} \times \boldsymbol{s}_{2,4}^{\mathrm{L}} \\ \boldsymbol{s}_{1,2}^{\mathrm{L}} \neq \boldsymbol{s}_{2,2}^{\mathrm{L}} \text{ or } \boldsymbol{r}_{s_{1,4}} \neq \boldsymbol{r}_{s_{2,4}} \end{cases} \tag{6}$$

Eq. (6) indicates that two PRU-type kinematic chains will produce only one equivalent constraint moment when satisfying: (1) the four vectors of $\boldsymbol{s}_{i,3}^{\mathrm{L}}$ and $\boldsymbol{s}_{i,4}^{\mathrm{L}}$ $(i=1,2)$ are coplanar; (2) $\boldsymbol{s}_{1,2}^{\mathrm{L}}$ and $\boldsymbol{s}_{2,2}^{\mathrm{L}}$ are non-parallel, or $\boldsymbol{s}_{1,4}^{\mathrm{L}}$ and $\boldsymbol{s}_{2,4}^{\mathrm{L}}$ are non-intersecting. Under the former condition, $\boldsymbol{s}_{2,3}^{\mathrm{L}}$ and $\boldsymbol{s}_{2,4}^{\mathrm{L}}$ can be expressed by

$$\begin{cases} \boldsymbol{s}_{2,3}^{\mathrm{L}} = a_1 \boldsymbol{s}_{1,3}^{\mathrm{L}} + b_1 \boldsymbol{s}_{1,4}^{\mathrm{L}} \\ \boldsymbol{s}_{2,4}^{\mathrm{L}} = a_2 \boldsymbol{s}_{1,3}^{\mathrm{L}} + b_2 \boldsymbol{s}_{1,4}^{\mathrm{L}} \end{cases} \tag{7}$$

where a_k and b_k (k=1, 2) denote any real number with $a_1a_2+b_1b_2=0$. This circumstance can be graphically illustrated by a 1UPR-1RPU combination as shown in Fig. 2 (b), where a UPR kinematic chain and a RPU kinematic chain are arranged with $\boldsymbol{s}_{1,3}^{\mathrm{L}} \,/\!/\, \boldsymbol{s}_{2,4}^{\mathrm{L}}$ and $\boldsymbol{s}_{1,4}^{\mathrm{L}} \,/\!/\, \boldsymbol{s}_{2,3}^{\mathrm{L}}$.

For case 3: the two constraint forces and the two constraint moments are equivalent constraints simultaneously. For such a case, there exists

$$\begin{cases} [\boldsymbol{s}_{1,2}^{\mathrm{L}}; \boldsymbol{r}_{s_{1,4}} \times \boldsymbol{s}_{1,2}^{\mathrm{L}}] = [\boldsymbol{s}_{2,2}^{\mathrm{L}}; \boldsymbol{r}_{s_{2,4}} \times \boldsymbol{s}_{2,2}^{\mathrm{L}}] \\ [\boldsymbol{0}; \boldsymbol{s}_{1,3}^{\mathrm{L}} \times \boldsymbol{s}_{1,4}^{\mathrm{L}}] = [\boldsymbol{0}; \boldsymbol{s}_{2,3}^{\mathrm{L}} \times \boldsymbol{s}_{2,4}^{\mathrm{L}}] \end{cases} \tag{8}$$

Eq. (8) can be rewritten as the following

$$\begin{cases} \boldsymbol{s}_{1,2}^{\mathrm{L}} = \boldsymbol{s}_{2,2}^{\mathrm{L}} \\ \boldsymbol{r}_{s_{1,4}} \times \boldsymbol{s}_{1,2}^{\mathrm{L}} = \boldsymbol{r}_{s_{2,4}} \times \boldsymbol{s}_{2,2}^{\mathrm{L}} \\ \boldsymbol{s}_{1,3}^{\mathrm{L}} \times \boldsymbol{s}_{1,4}^{\mathrm{L}} = \boldsymbol{s}_{2,3}^{\mathrm{L}} \times \boldsymbol{s}_{2,4}^{\mathrm{L}} \end{cases} \tag{9}$$

Eq. (9) implies that two PRU-type kinematic chains will generate an over-constraint force and an over-constraint moment simultaneously when satisfying: (1) $\boldsymbol{s}_{1,4}^{\mathrm{L}}$ and $\boldsymbol{s}_{2,4}^{\mathrm{L}}$ are collinear; (2) $\boldsymbol{s}_{1,2}^{\mathrm{L}}$ and $\boldsymbol{s}_{2,2}^{\mathrm{L}}$ are parallel. This can be graphically illustrated by a 2UPR combination as shown in Fig. 2 (c).

2.2. Type synthesis of 1T2R RAPMs with PRU-type kinematic chain

In this subsection, a screw theory based type synthesis for 1T2R RAPMs only with PRU-type kinematic chain is carried out.

According to the screw theory [39, 43, 44], the dot product of a twist screw and a wrench screw is equal to zero. This means that the rotational axes of a parallel mechanism are perpendicular to their constraint moments. Thus, for a 1T2R parallel mechanism with non-parallel rotational axes, at most one constraint moment is allowed in its wrench system. Since one PRU-type kinematic chain generates one constraint moment, two PRU-type kinematic chains in a 1T2R RAPM system should be combined in the form of either case 2 or case 3 to ensure that only one linearly independent constraint moment is produced in the wrench system.

If two PRU-type kinematic chains are arranged in the form of case 2, they will produce two equivalent constraint moments and two linearly independent constraint forces according to Eq. (6) and Eq. (7). The two independent constraint forces may be either parallel to each other or unparallel to each other. When the two constraint forces are parallel, the RAPM will become a one rotation and two translations RAPM. When the two constraint forces are unparallel, the two PRU-type chains must have different topological configuration. This will destroy the structural symmetry of a RAPM.

Based on the above discussions, one may naturally conclude that two PRU-type kinematic chains should be arranged according to the rules as shown in case 3 to generate equivalent constraints. In such a way, the linearly independent wrench screws of a 2'PRU' closed loop (i.e., a closed loop consists of two PRU-type kinematic chains) can be given by

$$\begin{cases}\hat{\$}_{2'\mathrm{PRU}',1}=[\mathbf{0};\boldsymbol{s}_{i,3}^{\mathrm{L}}\times\boldsymbol{s}_{i,4}^{\mathrm{L}}]\\ \hat{\$}_{2'\mathrm{PRU}',2}=[\boldsymbol{s}_{i,2}^{\mathrm{L}};\boldsymbol{r}_{s_{i,4}}\times\boldsymbol{s}_{i,2}^{\mathrm{L}}]\end{cases}\tag{10}$$

where $\hat{\$}_{2'\mathrm{PRU}',k}$ (k=1, 2) denotes the k^{th} wrench screw of the 2'PRU' closed loop.

According to the screw theory, the twist system of an individual 2'PRU' closed loop can be derived as

$$\begin{cases}\$_{2'\mathrm{PRU}',1}=[\mathbf{0};\boldsymbol{s}_{i,4}^{\mathrm{L}}]\\ \$_{2'\mathrm{PRU}',2}=[\mathbf{0};\boldsymbol{s}_{i,3}^{\mathrm{L}}\times\boldsymbol{s}_{i,4}^{\mathrm{L}}]\\ \$_{2'\mathrm{PRU}',3}=[\boldsymbol{s}_{i,4}^{\mathrm{L}};\boldsymbol{r}_{s_{i,4}}\times\boldsymbol{s}_{i,4}^{\mathrm{L}}]\\ \$_{2'\mathrm{PRU}',4}=[\boldsymbol{s}_{i,2}^{\mathrm{L}};\mathbf{0}]\end{cases}\tag{11}$$

where $\hat{\$}_{2'\mathrm{PRU}',k}$ (k=1 ,2 ,3 ,4) denotes the k^{th} twist screw of the 2'PRU' closed loop.

Note that a 2'PRU' closed loop produces two equivalent constraint forces and two equivalent constraint moments. The rest of kinematic chains in a RAPM are expected to produce only one linearly independent constraint forces. As can be derived from Eq. (11), when a screw with zero pitch is introduced into the original twist system, the 2'PRU' closed loop will lose its constraint moments. Therefore, adding an additional revolute joint to the end of a 2'PRU' closed loop will only generate a constraint force. Assume that the unit vector of $\boldsymbol{s}_{\mathrm{R}}^{\mathrm{L}}$ along the axis of the additional revolute joint is perpendicular and intersects with $\boldsymbol{s}_{i,4}^{\mathrm{L}}$ (i=1, 2). Thus, its twist screw can be expressed as

$$\$_{\mathrm{R}}=[\boldsymbol{s}_{\mathrm{R}}^{\mathrm{L}};\boldsymbol{r}_{O1}^{\mathrm{L}}\times\boldsymbol{s}_{\mathrm{R}}^{\mathrm{L}}]\tag{12}$$

where $\boldsymbol{r}_{O1}^{\mathrm{L}}$ is the position vector of the intersection point of $\boldsymbol{s}_{\mathrm{R}}^{\mathrm{L}}$ and $\boldsymbol{s}_{i,4}^{\mathrm{L}}$ measured in O_g-$x_g y_g z_g$.

Eq. (11) and Eq. (12) form the twist system of a (2'PRU')R kinematic chain. Using the screw theory again, one may derive the linearly independent wrench system of a (2'PRU')R kinematic chain as

$$\hat{\$}_{(2'\mathrm{PRU}')\mathrm{R}}=[\boldsymbol{s}_{i,2}^{\mathrm{L}};\boldsymbol{r}_{O1}^{\mathrm{L}}\times\boldsymbol{s}_{i,2}^{\mathrm{L}}]\quad(i=3,\ 4)\tag{13}$$

According to the screw theory, the mobility of a parallel mechanism is constrained by its all kinematic chain systems. Thus, the wrench system of a RAPM consisting of a 2'PRU' closed loop and a (2'PRU')R kinematic chain can be given by

$$\begin{cases}\hat{\$}_{\mathrm{RAPM},1}=[\mathbf{0};\boldsymbol{s}_{1,3}^{\mathrm{L}}\times\boldsymbol{s}_{1,4}^{\mathrm{L}}]\\ \hat{\$}_{\mathrm{RAPM},2}=[\mathbf{0};\boldsymbol{s}_{2,3}^{\mathrm{L}}\times\boldsymbol{s}_{2,4}^{\mathrm{L}}]\\ \hat{\$}_{\mathrm{RAPM},3}=[\boldsymbol{s}_{1,2}^{\mathrm{L}};\boldsymbol{r}_{s_{1,4}}\times\boldsymbol{s}_{1,2}^{\mathrm{L}}]\\ \hat{\$}_{\mathrm{RAPM},4}=[\boldsymbol{s}_{2,2}^{\mathrm{L}};\boldsymbol{r}_{s_{2,4}}\times\boldsymbol{s}_{2,2}^{\mathrm{L}}]\\ \hat{\$}_{\mathrm{RAPM},5}=[\boldsymbol{s}_{3,2}^{\mathrm{L}};\boldsymbol{r}_{O1}^{\mathrm{L}}\times\boldsymbol{s}_{3,2}^{\mathrm{L}}]\\ \hat{\$}_{\mathrm{RAPM},6}=[\boldsymbol{s}_{4,2}^{\mathrm{L}};\boldsymbol{r}_{O1}^{\mathrm{L}}\times\boldsymbol{s}_{4,2}^{\mathrm{L}}]\end{cases}\tag{14}$$

where $\hat{\$}_{\mathrm{RAPM},t}$ (t= 1-6) denotes the t^{th} wrench screw of such a RAPM. $\hat{\$}_{\mathrm{RAPM},1}$, $\hat{\$}_{\mathrm{RAPM},3}$, and $\hat{\$}_{\mathrm{RAPM},5}$ are equivalent to $\hat{\$}_{\mathrm{RAPM},2}$, $\hat{\$}_{\mathrm{RAPM},4}$, and $\hat{\$}_{\mathrm{RAPM},6}$, respectively.

By solving the reciprocal screws of Eq. (14), one may obtain three linearly independent twist screws of the RAPM with a 2'PRU' closed loop and a (2'PRU')R kinematic chain.

$$\begin{cases} \boldsymbol{\$}_{\mathrm{RAPM},1}^{\mathrm{m}} = [\mathbf{0}; \boldsymbol{s}_{i1,2}^{\mathrm{L}} \times \boldsymbol{s}_{i2,2}^{\mathrm{L}}] \\ \boldsymbol{\$}_{\mathrm{RAPM},2}^{\mathrm{m}} = [\boldsymbol{s}_{i2,2}^{\mathrm{L}}; \boldsymbol{r}_{\boldsymbol{s}_{i1,4}} \times \boldsymbol{s}_{i2,2}^{\mathrm{L}}] \quad (i1\text{=1, 2; } i2\text{=3, 4}) \\ \boldsymbol{\$}_{\mathrm{RAPM},3}^{\mathrm{m}} = [\boldsymbol{s}_{i1,2}^{\mathrm{L}}; \boldsymbol{r}_{O1}^{\mathrm{L}} \times \boldsymbol{s}_{i1,2}^{\mathrm{L}}] \end{cases} \tag{15}$$

where $\boldsymbol{\$}_{\mathrm{RAPM},1}^{\mathrm{m}}$ represents a twist screw perpendicular to both $\boldsymbol{s}_{i1,2}^{\mathrm{L}}$ and $\boldsymbol{s}_{i2,2}^{\mathrm{L}}$; $\boldsymbol{\$}_{\mathrm{RAPM},2}^{\mathrm{m}}$ denotes a twist passing through any point on the vector $\boldsymbol{s}_{i1,4}^{\mathrm{L}}$ and parallel to $\boldsymbol{s}_{i2,2}^{\mathrm{L}}$; $\boldsymbol{\$}_{\mathrm{RAPM},3}^{\mathrm{m}}$ is a twist parallel to $\boldsymbol{s}_{i1,2}^{\mathrm{L}}$ and passing through the intersection point of $\boldsymbol{s}_{\mathrm{R}}^{\mathrm{L}}$ and $\boldsymbol{s}_{i1,4}^{\mathrm{L}}$.

Eq. (15) indicates that a 1T2R RAPM can be constructed by composing a 2'PRU' closed loop and a (2'PRU')R kinematic chain. Such kinds of RAPMs possess two continuous rotational axes, which are located close to the universal joint of the 2'PRU'closed loop and the (2'PRU')R kinematic chain, respectively. Following this track, a family of potential 1T2R RAPMs with only PRU-type chains can be synthesized, whose tree diagrams of possible joint sequences are demonstrated in Fig. 3. For the sake of illustration, the synthesized 1T2R RAPMs can be further divided into three categories: UP-equivalent RAPM, PU-equivalent RAPM and RPR-equivalent RAPM [23]. Herein, MP, MP1/ MP2, B, and B1/ B2 denote a moving platform, a subsidiary moving platform, a base and a subsidiary base, respectively. 'P', 'R' and 'U' represent a prismatic joint, a revolute joint and a universal joint, respectively.

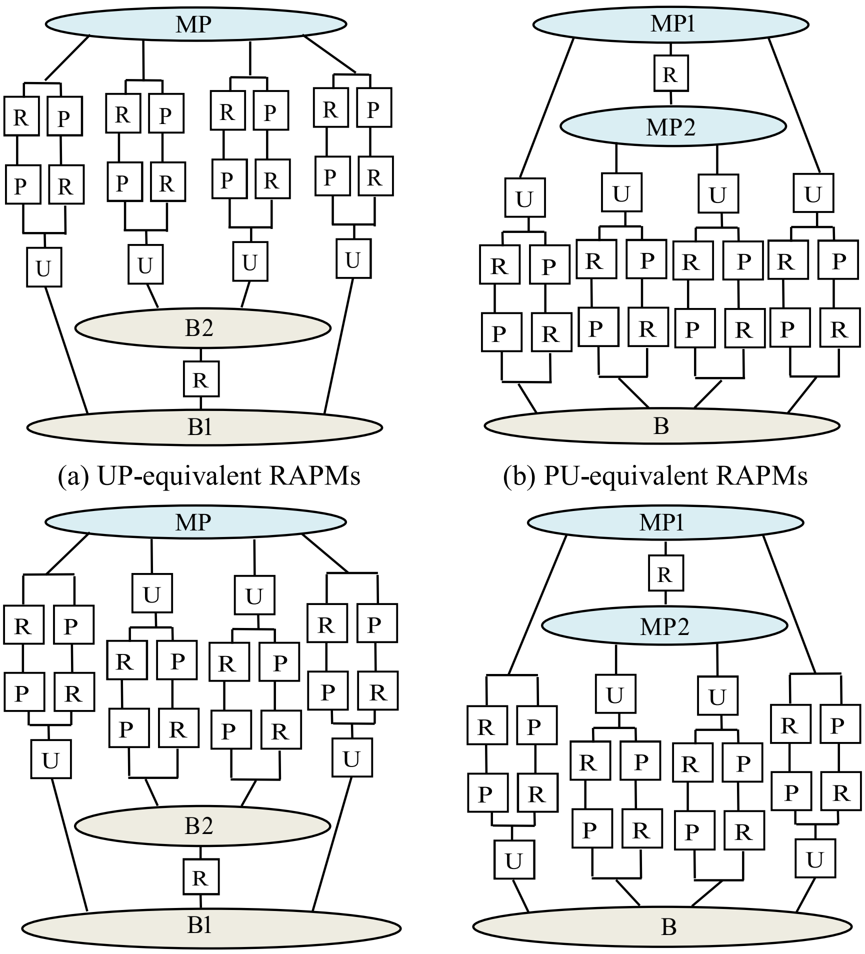

(a) UP-equivalent RAPMs (b) PU-equivalent RAPMs

(c) RPR-equivalent RAPMs

Fig. 3 Tree diagrams of joint sequences of synthesized 1T2R RAPMs

As can be seen from Fig. 3, 9 kinds of UP-equivalent RAPMs, 9 kinds of PU-equivalent RAPMs and 12 kinds of RPR-equivalent RAPMs can be synthesized. For clarity, the topological architectures of these RAPMs are listed in Table 1. Herein, 'P', 'R' and 'U' represent a prismatic joint, a revolute joint and a universal joint, respectively.

Table 1 The topological architectures of the synthesized 1T2R RAPMs

Type	Topological architecture		
UP-equivalent RAPM	2UPR-(2UPR)R	2URP-(2URP)R	2UPR-(2URP)R
	2RPU-(2PRU)R	1PRU-1RPU-(2PRU)R	2PRU-(1PRU-1RPU)R
	1UPR-1URP-(2URP)R	2URP-(1UPR-1URP)R	1UPR-1URP-(1UPR-1URP)R
PU-equivalent RAPM	2PRU-(2PRU)R	2RPU-(2RPU)R	2PRU-(2RPU)R
	2URP-(2UPR)R	1UPR-1URP-(2UPR)R	2UPR-(1UPR-1URP)R
	1PRU-1RPU-(2RPU)R	2RPU-(1PRU-1RPU)R	1PRU-1RPU-(1PRU-1RPU)R
RPR-equivalent RAPM	2PRU-(2UPR)R	2UPR-(2PRU)R	2RPU-(2URP)R
	2URP-(2RPU)R	1PRU-1RPU-(2UPR)R	2UPR-(1PRU-1RPU)R
	1UPR-1URP-(2PRU)R	2PRU-(1UPR-1URP)R	1UPR-1URP-(2RPU)R
	2RPU-(1UPR-1URP)R	1PRU-1RPU-(1UPR-1URP)R	1UPR-1URP-(1PRU-1RPU)R

As highlighted in Table 1, there are four types of 1T2R RAPM with identical kinematic chain configuration, whose topological architectures are 2UPR-(2UPR)R, 2URP-(2URP)R, 2PRU-(2PRU)R, and 2RPU-(2RPU)R, respectively. Among these four RAPMs, the 2PRU-(2PRU)R RAPM is selected as a candidate for 1T2R spindle head to construct 5-axis hybrid machine tools in the present study. The reason lies in that the four actuated joints fixed to the base is beneficial for reducing rotatory inertia and improving dynamic response of a parallel manipulator [37, 45, 46].

3. Conceptual design and kinematic analysis

In this section, a novel hybrid machine tool is constructed by integrating a newly invented spindle head with a two-sliding gantry. The invented spindle head is featured by four symmetrically arranged PRU limbs, making it possessing the merits of symmetrical kinematic performance and large orientation workspace. In addition, the inverse/ forward position and the singularity of the proposed hybrid machine tool are analyzed to reveal its fundamental kinematic performances.

3.1. Conceptual design

Based on the above selected 2PRU-(2PRU)R RAPM, a conceptual design of 1T2R spindle head is conducted. For expression convenience, this type of spindle head is named as RAVASH abbreviating for redundantly actuated virtual-axis spindle head. The Structural arrangement and the schematic diagram of RAVASH are depicted in Fig. 4.

As shown in Fig. 4 (a), the RAVASH consists of a base, a dual platform and four identical PRU kinematic chains. To be specific, MP1 and MP2 are two individual platforms of the dual platform connected through a revolute joint. The spindle is connected to MP1 and through the dual platform. Limb 1, limb 2, limb 3 and limb 4 are four symmetrically arranged PRU kinematic chains. Limb 1 and limb 3 connect MP1 to the base, while limb 2 and limb 4 connect MP2 to the base. Furthermore, each individual PRU kinematic chain contains a prismatic joint, a revolute joint and a universal joint. The prismatic joint is actuated by a servo motor via a ball screw and two guide rails. The universal joint is designed as two revolute joints with perpendicularly intersecting axes for a compact conformation.

As shown in Fig. 4 (b), B_i represents the origin of the i^{th} prismatic joint where a servo motor is mounted. A_i and C_i (i=1-4) are the geometric centers of universal joint and revolute joint, respectively. O is the central point of the quadrate of $\square B_1B_2B_3B_4$, while O_0 and O_1 denote the midpoints of the segments of A_1A_2 and A_3A_4, respectively. P represents the tool tip of the spindle. The length of A_1A_2 or A_3A_4 is $2r_a$; the length of B_1B_2 or B_3B_4 is $2r_b$; the length of C_iA_i is l; the length of B_iC_i is d_i, the length of PO_0 is d_P and the length of O_0O_1 is d_e. To facilitate kinematic analysis, some the following coordinate systems are defined. A reference coordinate system O-xyz is established at point O, with x axis pointing to B_3, y axis pointing to B_2 and z axis satisfying the right-hand rule. A moving coordinate system O_0-uvw is set at point O_0, with u axis pointing to A_2, w axis perpendicular to A_1A_2 and A_3A_4, v axis satisfying the right-hand rule. In addition, a local coordinate system O_1-$u_1v_1w_1$ is set at point O_1, with v_1 axis pointing to A_3, w_1 axis parallel to w axis and u_1 axis satisfying the right-hand rule.

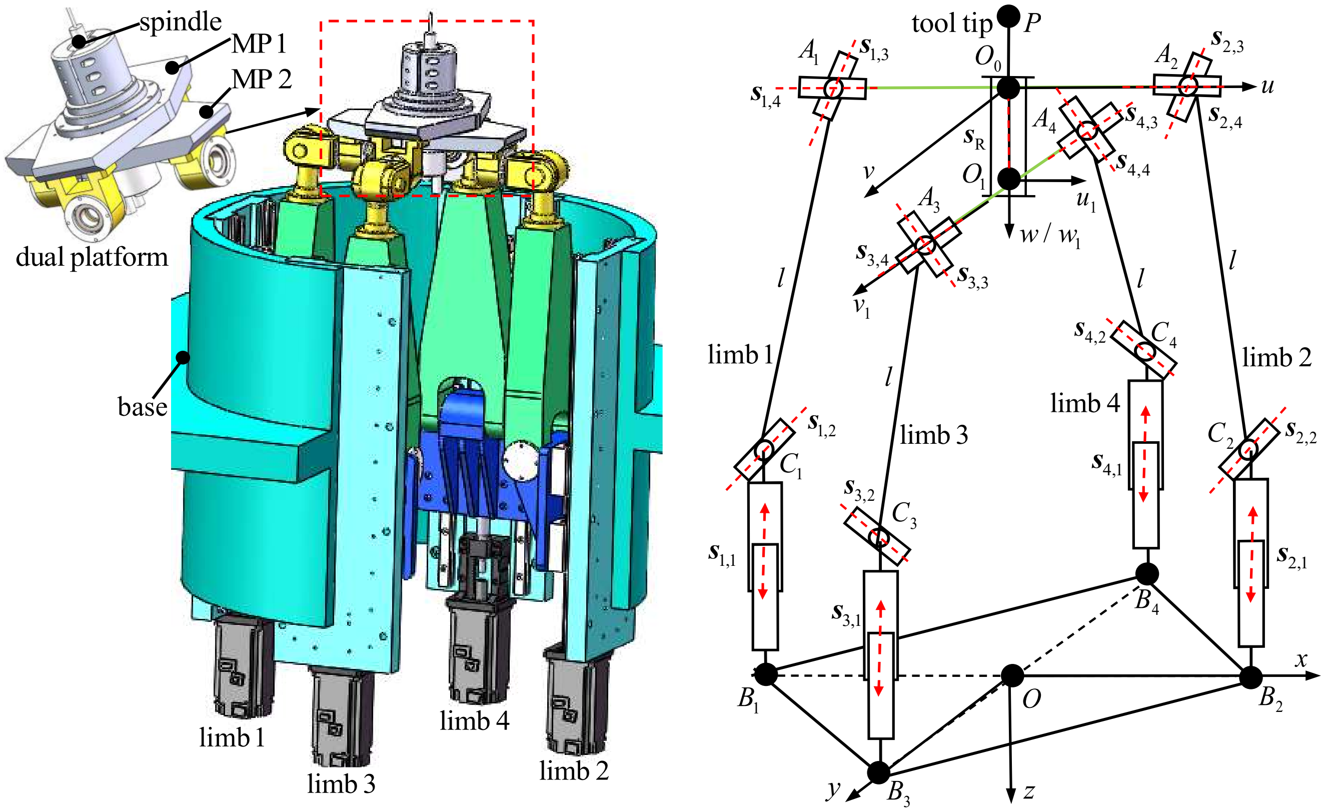

(a) Conceptual design (b) Schematic diagram

Fig. 4 Conceptual design and schematic diagram of the RAVASH

Letting $s_{i,j}$ denotes a unit vector along the j^{th} single-DOF joint axis of the i^{th} limb, and s_R represents the unit vector along the axis of revolute joint connecting MP1 and MP2. The geometrical constraints of the proposed RAVASH can be described as follows.

1) s_R is perpendicular and intersects with $s_{1,4}$ and $s_{3,4}$.
2) $s_{1,2}$, $s_{1,3}$, $s_{2,2}$, and $s_{2,3}$ are parallel to each other.
3) $s_{3,2}$, $s_{3,3}$, $s_{4,2}$, and $s_{4,3}$ are parallel to each other.
4) $s_{1,1}$, $s_{2,1}$, $s_{3,1}$, and $s_{4,1}$ are parallel to z axis.
5) $s_{1,4}$ and $s_{2,4}$, are collinear while $s_{3,4}$ and $s_{4,4}$ are collinear.
6) $s_{i,3}$ is perpendicular to $s_{i,4}$ (i=1-4).
7) $s_{i,2}$ is perpendicular to $s_{j,2}$ (i=1, 3; j=2, 4).

By integrating the above RAVASH, a novel hybrid machine tool with 5-axis machining capability is constructed. Fig. 5 demonstrates a virtual prototype of the constructed 5-axis hybrid machine tool.

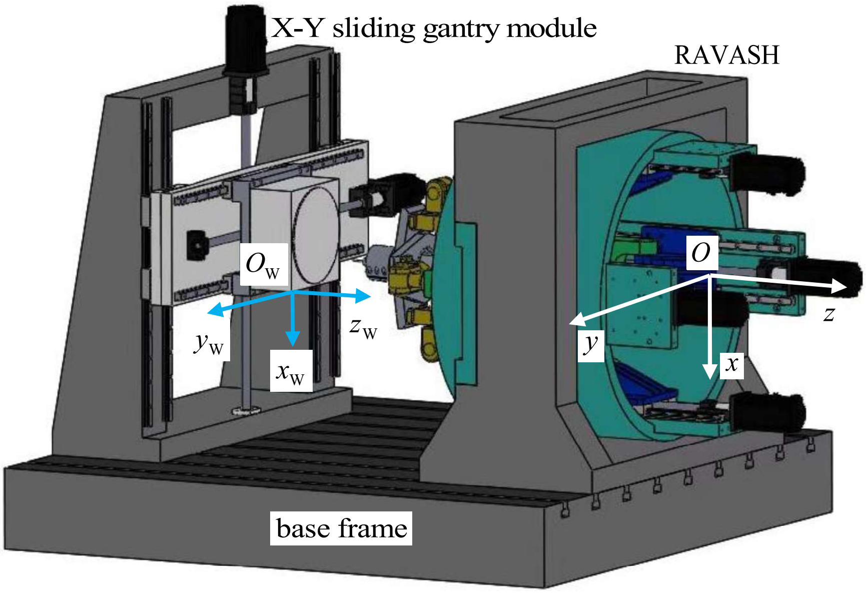

Fig. 5 A virtual prototype of the proposed 5-axis machine tool

As shown in Fig. 5, the proposed hybrid machine tool is designed as a horizontal-type arrangement, which consists of a RAVASH, an X-Y sliding gantry module and a base frame. Herein, the two rotational DOFs of the RAVASH are used as A/B virtual axes to adjust the orientation of the spindle. The X-Y sliding gantries and the translational DOF of the RAVASH are adopted as x, y, and z axes. For derivation facility, a workpiece coordinate system O_W-$x_W y_W z_W$ is established at the origin of the workpiece O_W with its three orthogonal axes parallel to those of the frame of O-xyz.

3.2. Inverse position solution

The inverse position solution of a hybrid machine tool refers to the determination of the displacements of actuated joints for a set of given position vector of tool tip and tool-axis unit vector. The inverse position solution of the proposed hybrid machine tool can be formulated based on the following two procedures:

Procedure 1. Deriving the inverse position formulations of the RAPM.

By adopting the z-y-x Euler angles, the transformation matrix $\boldsymbol{R}$ of the coordinate system O_0-uvw with respect to the coordinate system O-xyz can be written as

$$\boldsymbol{R}=\begin{bmatrix} \mathrm{c}\varphi\mathrm{c}\theta & \mathrm{c}\varphi\mathrm{s}\theta\mathrm{s}\psi-\mathrm{s}\varphi\mathrm{c}\psi & \mathrm{c}\varphi\mathrm{s}\theta\mathrm{c}\psi+\mathrm{s}\varphi\mathrm{s}\psi \\ \mathrm{s}\varphi\mathrm{c}\theta & \mathrm{s}\varphi\mathrm{s}\theta\mathrm{s}\psi+\mathrm{c}\varphi\mathrm{c}\psi & \mathrm{s}\varphi\mathrm{s}\theta\mathrm{c}\psi-\mathrm{c}\varphi\mathrm{s}\psi \\ -\mathrm{s}\theta & \mathrm{s}\psi\mathrm{c}\theta & \mathrm{c}\theta\mathrm{c}\psi \end{bmatrix} \tag{16}$$

Where ψ, θ and φ are the Euler angles, i.e. precession angle, nutation angle and rotation angle; 's' and 'c' mean 'cosine' and 'sine' functions, respectively.

Measured in the frame of O-xyz, the position vectors $\boldsymbol{r}_{bi}$ of point B_i (i=1-4) can be given by

$$\boldsymbol{r}_{b1}=[-r_b,0,0]^{\mathrm{T}},\ \boldsymbol{r}_{b2}=[r_b,0,0]^{\mathrm{T}},\ \boldsymbol{r}_{b3}=[0,r_b,0]^{\mathrm{T}},\ \boldsymbol{r}_{b4}=[0,-r_b,0]^{\mathrm{T}} \tag{17}$$

Measured in the frame of O_0-uvw, the position vector $\boldsymbol{r}_{0,ai}$ of point A_i (i=1-4) can be expressed as

$$\boldsymbol{r}_{0,a1}=[-r_a,0,0]^{\mathrm{T}},\ \boldsymbol{r}_{0,a2}=[r_a,0,0]^{\mathrm{T}},\ \boldsymbol{r}_{0,a3}=\frac{r_a(\boldsymbol{s}_{\mathrm{R}}\times\boldsymbol{s}_{3,2})}{|\boldsymbol{s}_{\mathrm{R}}\times\boldsymbol{s}_{3,2}|},\ \boldsymbol{r}_{0,a4}=\frac{r_a(\boldsymbol{s}_{\mathrm{R}}\times\boldsymbol{s}_{4,2})}{|\boldsymbol{s}_{\mathrm{R}}\times\boldsymbol{s}_{4,2}|} \tag{18}$$

where $\boldsymbol{s}_{\mathrm{R}}$=[0,0,-1]$^{\mathrm{T}}$, $\boldsymbol{s}_{3,2}$=$\boldsymbol{R}^{-1}$[-1,0, 0]$^{\mathrm{T}}$, and $\boldsymbol{s}_{4,2}$=$\boldsymbol{R}^{-1}$[1,0, 0]$^{\mathrm{T}}$.

Measured in the frame of O-xyz, the vector of $\boldsymbol{r}_{ai}$ pointing from O_0 to A_i can be formulated as

$$\boldsymbol{r}_{a1}=\boldsymbol{R}\boldsymbol{r}_{0,a1},\ \boldsymbol{r}_{a2}=\boldsymbol{R}\boldsymbol{r}_{0,a2},\ \boldsymbol{r}_{a3}=\boldsymbol{R}\boldsymbol{r}_{0,a3},\ \boldsymbol{r}_{a4}=\boldsymbol{R}\boldsymbol{r}_{0,a4} \tag{19}$$

According to the aforementioned geometrical constraints of the RAVASH, one may obtain the constraint

Eq.s as the follows

$$s_{i,2}s_{i,4}=0,\quad s_{i,2}r_{O0}=0,\quad s_{j,2}r_{O0}=0\quad (i=1,2;j=3,4) \tag{20}$$

where $\boldsymbol{r}_{O0}=[x, y, z]^{\mathrm{T}}$ is the position vectors of O_0 measured in the frame of O-xyz.

Taking ψ, θ, and z as independent posture parameters, the parasitic motions of the platform can be calculated by solving Eq. (20)

$$x=0,\quad y=0,\quad \varphi=0 \tag{21}$$

Eq. (21) shows that the proposed 2PRU-(2PRU)R RAPM has no parasitic motion. This indicates that the RAPM possesses the merits of simple kinematic, easy control and easy calibration [23, 39].

Once ψ, θ, and z are given, the length of B_iA_i (q_i) and its unit direction vector ($\boldsymbol{v}_{qi}$) can be calculated by Eq. (22) and Eq. (23), respectively.

$$q_i=|\boldsymbol{r}_{O0}+\boldsymbol{r}_{ai}-\boldsymbol{r}_{bi}|\quad (i=1\text{-}4) \tag{22}$$

$$\boldsymbol{v}_{qi}=(\boldsymbol{r}_{O0}+\boldsymbol{r}_{ai}-\boldsymbol{r}_{bi})/q_i\quad (i=1\text{-}4) \tag{23}$$

According to the cosine law, the three sides of triangle $\Delta B_iC_iA_i$ (i=1-4) satisfy

$$l^2=d_i^2+q_i^2-2d_iq_i\cos(\theta_i)\quad (i=1\text{-}4) \tag{24}$$

where $\cos(\theta)=\boldsymbol{v}_{di}\boldsymbol{v}_{qi}$; $\boldsymbol{v}_{di}=[0,0,-1]^{\mathrm{T}}$ denotes the unit direction vector of the i^{th} actuated prismatic joint.

By solving Eq. (24), one may obtain the two potential solutions of the actuators' displacement d_i

$$\begin{cases} d_{i1}=q_i\cos(\theta_i)-\sqrt{(q_i\cos(\theta_i))^2-(q_i^2-l^2)} \\ d_{i2}=q_i\cos(\theta_i)+\sqrt{(q_i\cos(\theta_i))^2-(q_i^2-l^2)} \end{cases}\quad (i=1\text{-}4) \tag{25}$$

The results can be illustrated by Fig. 6 in which two potential positions of C_i are obtained by drawing a circle with a radius of l at A_i to form the triangle $\Delta B_iC_iA_i$ (i=1-4).

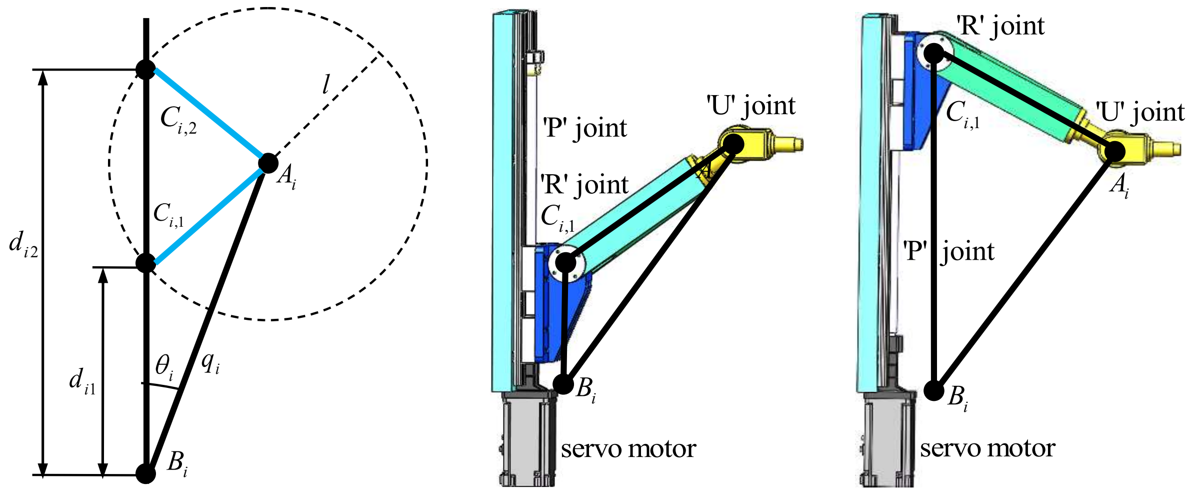

(a) Solution of d_i by using graphical method (b) Expanded installation mode (c) Folded installation mode

Fig. 6 The diagram of two solutions of d_i

As shown in Fig. 6 (a), two potential positions of C_i are obtained (i.e. the two intersections C_{i1} and C_{i2} of the line along $\boldsymbol{v}_{di}$ and the circle at A_i). This is coincident with the results of Eq. (25). Herein, d_{i1} and d_{i2} are the solutions of C_i locating at C_{i1} and C_{i2}, respectively. In a physical sense, it indicates that an individual kinematic chain has two types of installation modes as the follows:

(1) Expanded installation mode: the angle $\angle B_iC_iA_i$ is an obtuse angle as shown in Fig. 6 (b).

(2) Folded installation mode: the angle $\angle B_iC_iA_i$ is an acute angle as shown in Fig. 6 (c).

Specially, the configuration of the i^{th} limb is under the transition state from the expanded installation mode to the folded installation mode when $\angle B_iC_iA_i=90°$.

Procedure 2. Deriving the inverse position formulations between the parallel and the serial modules.

Measured in the frame of *O-xyz*, the position vector $\boldsymbol{r}_P$ of the tool tip *P* can be given by

$$\boldsymbol{r}_P = \boldsymbol{r}_{O0} + \boldsymbol{R}[0,0,-d_{\mathrm{P}}]^{\mathrm{T}} \tag{26}$$

By considering the motion relationship between the parallel and the serial modules, the position vector $\boldsymbol{r}_P$ of the tool tip *P* measured in *O-xyz* can be expressed as

$$\boldsymbol{r}_P = \boldsymbol{r}_{O\mathrm{w}} + \boldsymbol{R}_1 \boldsymbol{r}_P^{\mathrm{W}} \tag{27}$$

where $\boldsymbol{r}_{O\mathrm{w}}=[x_{O\mathrm{w}}, y_{O\mathrm{w}}, z_{O\mathrm{w}}]$ denotes the position vector of the workpiece origin O_{W} measured in *O-xyz*; $\boldsymbol{r}_P^{\mathrm{W}} = [x_P^{\mathrm{W}}, y_P^{\mathrm{W}}, z_P^{\mathrm{W}}]^{\mathrm{T}}$ denotes the position vector of the tool tip measured in O_{W}-$x_{\mathrm{W}}y_{\mathrm{W}}z_{\mathrm{W}}$. $\boldsymbol{R}_1$ is the transformation matrix $\boldsymbol{R}_1$ of the coordinate system O_{W}-$x_{\mathrm{W}}y_{\mathrm{W}}z_{\mathrm{W}}$ with respect to the coordinate system *O-xyz*

$$\boldsymbol{R}_1 = \begin{bmatrix} 1 & 0 & 0 \\ 0 & 1 & 0 \\ 0 & 0 & 1 \end{bmatrix} \tag{28}$$

By substituting Eq. (26) into Eq. (27), one may obtain

$$\boldsymbol{r}_P = \boldsymbol{r}_{O\mathrm{w}} + \boldsymbol{R}_1 \boldsymbol{r}_P^{\mathrm{W}} = \boldsymbol{r}_{O0} + \boldsymbol{R}[0,0,-d_e]^{\mathrm{T}} \tag{29}$$

The tool-axis unit vector $\boldsymbol{t}_e$ measured in the frame *O-xyz* can be given by

$$\boldsymbol{t}_e = \boldsymbol{R}_1 \boldsymbol{t}_e^{\mathrm{W}} = \boldsymbol{R}[0,0,-1]^{\mathrm{T}} \tag{30}$$

where $\boldsymbol{t}_e^{\mathrm{W}} = [x_{te}, y_{te}, z_{te}]^{\mathrm{T}}$ is the tool-axis unit vector measured in O_{W}-$x_{\mathrm{W}}y_{\mathrm{W}}z_{\mathrm{W}}$.

And there exists

$$\psi = \arcsin(y_{te}),\quad \theta = \arctan(\frac{x_{te}}{z_{te}}) \tag{31}$$

By substituting Eq. (31) into Eq. (29), one may obtain

$$z = z_{O\mathrm{w}} + z_P^{\mathrm{W}} + d_e \cos(\psi)\cos(\theta) \tag{32}$$

By combining Eq. (22) with Eqs. (29)-(32), one may derive the inverse position solution of the proposed 5-axis machine tool as

$$\begin{cases} d_i = q_i \cos(\theta_i) - \sqrt{(q_i \cos(\theta_i))^2 - (q_i^2 - l^2)} \ \ (i = 1-4) \\ d_5 = -d_e \cos(\psi)\sin(\theta),\ d_6 = d_e \sin(\psi) \end{cases} \tag{33}$$

where d_5 and d_6 are the displacements of the X sliding gantry and the Y sliding gantry, respectively. And there exists

$$q_i = \left| \boldsymbol{r}_{O\mathrm{w}} + \boldsymbol{R}_1 \boldsymbol{r}_P^{\mathrm{W}} - \boldsymbol{R} d_e [0,0,-1]^{\mathrm{T}} + \boldsymbol{r}_{ai} - \boldsymbol{r}_{bi} \right| \tag{34}$$

3.3. Forward position solution

The forward position solution of the constructed hybrid machine tool refers to the determination of the position vector of tool tip and the tool-axis unit vector for a set of given displacements of actuated joints.

By substituting Eq. (17), Eq. (19), and Eq. (22) into Eq. (25), one may obtain the followings

$$d_1^2 + 2d_1(z + r_a \sin\theta) - l^2 + (r_b - r_a\cos\theta)^2 + (z + r_a \sin\theta)^2 = 0 \tag{35-1}$$

$$d_2^2 + 2d_2(z - r_a \sin\theta) - l^2 + (r_b - r_a\cos\theta)^2 + (z - r_a \sin\theta)^2 = 0 \tag{35-2}$$

$$d_3^2 + 2d_3(z + \frac{r_a \sin\psi}{G_1}) - l^2 + (\frac{G_2}{G_1} - r_b)^2 + (z + \frac{r_a \sin\psi}{G_1})^2 = 0 \tag{35-3}$$

$$d_4^2 + 2d_4(z - \frac{r_a \sin\psi}{G_1}) - l^2 + (r_b - \frac{G_2}{G_1})^2 + (z - \frac{r_a \sin\psi}{G_1})^2 = 0 \tag{35-4}$$

where $G_1 = \sqrt{(\cos\theta\cos\psi)^2 + (\sin\psi)^2}$, $G_2 = r_a\cos\theta\cos\psi$.

When limb 1 and limb 2 are both under the transition state, it will lead to $d_1=d_2=-z$ and $r_b=r_a+l$. By solving Eq. (35-1) or Eq. (35-2), the nutation angle θ can be obtained as

$$\theta = 0° \tag{36}$$

When one of limb 1 and limb 2 is assembled in an expanded installation mode or a folded installation mode, it will lead to $(d_1+d_2+2z)<0$ or $(d_1+d_2+2z)>0$, respectively.

Combining Eq. (35-1) and Eq. (25-2), one may obtain

$$(d_1 - d_2 + 2r_a \sin\theta)(d_1 + d_2 + 2z) = 0 \tag{37}$$

By solving Eq. (38), the nutation angle θ can be expressed as

$$\theta = \arcsin\left(\frac{d_2 - d_1}{2r_a}\right) \tag{38}$$

When limb 3 and limb 4 are both under the transition state, it will lead to $d_3=d_4=-z$ and $r_b=r_a+l$. By solving Eq. (35-3) or Eq. (35-4), the precession angle ψ an be obtained as

$$\psi = 0° \tag{39}$$

When one of limb 3 and limb 4 is assembled in an expanded installation mode or a folded installation mode, it will lead to $(d_3+d_4+2z)<0$ or $(d_3+d_4+2z)>0$, respectively.

Combining Eq. (35-3) or Eq. (35-4), one may obtain

$$\left(d_3 - d_4 + \frac{2r_a \mathrm{s}\psi}{\sqrt{(\mathrm{c}\theta\mathrm{c}\psi)^2 + (\mathrm{s}\psi)^2}}\right)(d_3 + d_4 + 2\mathrm{z}) = 0 \tag{40}$$

By solving Eq. (41), the precession angle ψ can be obtained as

$$\psi = \mathrm{sign}(d_4 - d_3)\arctan\sqrt{\frac{k(\cos\theta)^2}{1-k}}\ ,\quad k = \left(\frac{d_4 - d_3}{2r_a}\right)^2 \tag{41}$$

where 'sign(*)' means signum function.

By substituting Eq. (38) and Eq. (41) into Eq. (26), one may obtain two solutions of z

$$z_1 = \frac{-t_3 - \sqrt{t_3^2 - 4t_4}}{4}\ ,\quad z_2 = \frac{-t_3 + \sqrt{t_3^2 - 4t_4}}{4} \tag{42}$$

where

$$t_3 = 2d_1 + 2r_a \sin\theta\ ,\quad t_4 = (d_1 + r_a \sin\theta)^2 - l^2 + (r_b - r_a\cos\theta)^2 \tag{43}$$

The results can be illustrated by Fig. 7, in which the two potential positions of A_i can be obtained by drawing a circle with a radius of l at C_i to form triangle $\Delta B_iC_iA_i$ (i=1-4).

As shown in Fig. 7 (a), the two potential positions of A_i (i=1-4) can be obtained (i.e. A_{i1} and A_{i2}) at different heights after ψ and θ are calculated by Eq. (38) and Eq. (41). This indicates that the coordinate z has two solutions, which is coincident with the results of Eq. (42). For the sake of physical clarity, two typical installation modes may be addressed as the follows:

(1) Upward installation mode: the four limbs of the RAVASH are all assembled in expanded installation mode as shown in Fig. 7 (b).

(2) Downward installation mode: the four limbs of the RAVASH are all assembled in folded installation mode as shown in Fig. 7 (c).

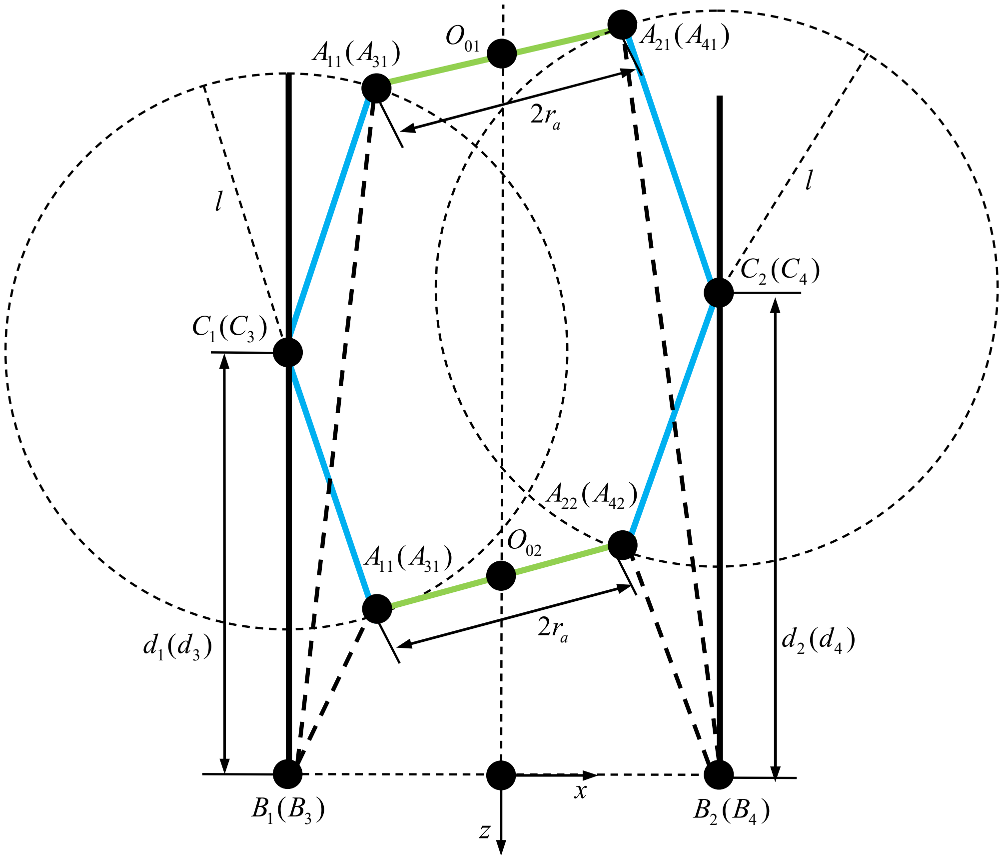

(a) The solution of z by using graphical method

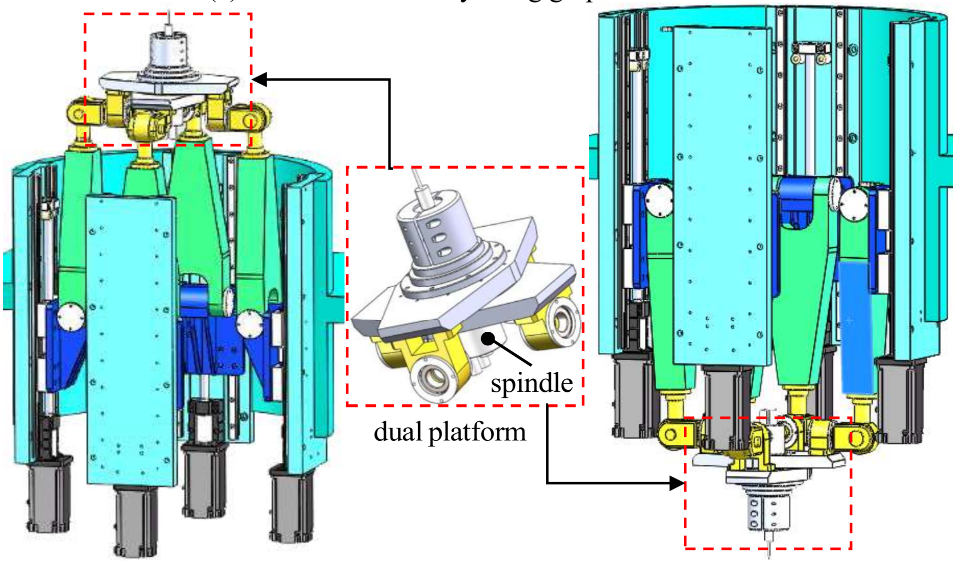

(b) Upward installation mode (c) Downward installation mode

Fig. 7 The diagram of two solutions of z

To avoid collision and movement interference between the servo motors and the universal joints, the upward installation mode is adopted in the present study to construct the RAVASH as shown in Fig. 5.

By substituting ψ, θ, z, d_5 and d_6 into Eq. (29) and Eq. (30), the position vector of the tool tip $\boldsymbol{r}_P^{\mathrm{W}}$ and the tool-axis unit vector $\boldsymbol{t}_e^{\mathrm{W}}$ can be solved as

$$\boldsymbol{r}_P^{\mathrm{W}} = [-d_e \sin\theta\cos\psi - d_5, d_e \sin\psi, -d_e\cos\theta\cos\psi - z_{O\mathrm{w}}]^{\mathrm{T}} \tag{44}$$

$$\boldsymbol{t}_e = [-\sin\theta\cos\psi, \sin\psi, -\cos\theta\cos\psi]^{\mathrm{T}} \tag{45}$$

3.4. Singularity analysis

Since the tool (the spindle) is connected to the platform of 1T2R parallel mechanism, the twist $\boldsymbol{\$}_{\mathrm{Tool}}$ of tool can be calculated by combining linearly all twists of the platform.

$$\begin{cases} \boldsymbol{\$}_{\mathrm{Tool}} = v_{\mathrm{d}}^{\mathrm{m}}\boldsymbol{\$}_{\mathrm{PM},1}^{\mathrm{m}} + v_{\theta 1}^{\mathrm{m}}\boldsymbol{\$}_{\mathrm{PM},2}^{\mathrm{m}} + v_{\theta 2}^{\mathrm{m}}\boldsymbol{\$}_{\mathrm{PM},3}^{\mathrm{m}} \\ \boldsymbol{\$}_{\mathrm{PM},1}^{\mathrm{m}} = [\mathbf{0}_{3\times 1} \ ; \ \boldsymbol{s}_1^{\mathrm{m}}] \\ \boldsymbol{\$}_{\mathrm{PM},2}^{\mathrm{m}} = [\boldsymbol{s}_2^{\mathrm{m}} \ ; \ \boldsymbol{r}_{O0}^{\mathrm{m}} \times \boldsymbol{s}_2^{\mathrm{m}}] \\ \boldsymbol{\$}_{\mathrm{PM},3}^{\mathrm{m}} = [\boldsymbol{s}_3^{\mathrm{m}} \ ; \ \boldsymbol{r}_{O0}^{\mathrm{m}} \times \boldsymbol{s}_3^{\mathrm{m}}] \end{cases} \tag{46}$$

where $\boldsymbol{\$}_{\mathrm{PM},1}^{\mathrm{m}}$, $\boldsymbol{\$}_{\mathrm{PM},2}^{\mathrm{m}}$, and $\boldsymbol{\$}_{\mathrm{PM},3}^{\mathrm{m}}$ are three twist screws of a 1T2R parallel mechanism. $\boldsymbol{s}_1^{\mathrm{m}}$, $\boldsymbol{s}_2^{\mathrm{m}}$, and $\boldsymbol{s}_3^{\mathrm{m}}$ represent unit vectors alone the translational or the rotational axes of 1T2R parallel mechanism. $\boldsymbol{r}_{O0}^{\mathrm{m}}$ is a position vectors pointing from tool tip to O_0. $v_{\mathrm{d}}^{\mathrm{m}}$, $v_{\theta 1}^{\mathrm{m}}$, and $v_{\theta 2}^{\mathrm{m}}$ denote the linear or the angular velocity of above three twist screws.

The workpiece is connected to the X-Y sliding gantries, the twist $\boldsymbol{\$}_{\mathrm{wp}}$ of workpiece can be defined as a linear combination of the X and the Y sliding gantries.

$$\begin{cases} \boldsymbol{\$}_{\mathrm{wp}} = v_{\mathrm{d1}}^{\mathrm{w}}\boldsymbol{\$}_{\mathrm{SM},1}^{2} + v_{\mathrm{d2}}^{\mathrm{w}}\boldsymbol{\$}_{\mathrm{SM},2}^{2} \\ \boldsymbol{\$}_{\mathrm{SM},1}^{2} = [\mathbf{0}_{3\times 1} \ ; \ \boldsymbol{s}_1^{\mathrm{w}}] \\ \boldsymbol{\$}_{\mathrm{SM},2}^{2} = [\mathbf{0}_{3\times 1} \ ; \ \boldsymbol{s}_2^{\mathrm{w}}] \end{cases} \tag{47}$$

where $\boldsymbol{\$}_{\mathrm{SM},1}^{\mathrm{w}}$ and $\boldsymbol{\$}_{\mathrm{SM},2}^{\mathrm{w}}$ are twist screws of the X and the Y sliding gantries, respectively. $v_{\mathrm{d1}}^{\mathrm{w}}$ and $v_{\mathrm{d2}}^{\mathrm{w}}$ denote the linear velocity of the X and the Y sliding gantries, respectively. $\boldsymbol{s}_1^{\mathrm{w}}$ and $\boldsymbol{s}_2^{\mathrm{w}}$ represent unit vectors alone the X and the Y sliding gantries, respectively.

The relative motion $\boldsymbol{\$}_{\mathrm{wp\text{-}Tool}}$ between the tool and the workpiece can be expressed as

$$\begin{aligned} &\boldsymbol{\$}_{\mathrm{wp\text{-}Tool}} = v_{\mathrm{d}}^{\mathrm{m}}\boldsymbol{\$}_{\mathrm{PM},1}^{\mathrm{m}} + v_{\theta 1}^{\mathrm{m}}\boldsymbol{\$}_{\mathrm{PM},2}^{\mathrm{m}} + v_{\theta 2}^{\mathrm{m}}\boldsymbol{\$}_{\mathrm{PM},3}^{\mathrm{m}} + v_{\mathrm{d1}}^{\mathrm{w}}\boldsymbol{\$}_{\mathrm{SM},1}^{2} + v_{\mathrm{d2}}^{\mathrm{w}}\boldsymbol{\$}_{\mathrm{SM},2}^{2} = \\ &\begin{bmatrix} \mathbf{0}_{3\times 1} & \boldsymbol{s}_2^{\mathrm{m}} & \boldsymbol{s}_3^{\mathrm{m}} & \mathbf{0}_{3\times 1} & \mathbf{0}_{3\times 1} \\ \boldsymbol{s}_1^{\mathrm{m}} & \boldsymbol{r}_{O0}^{\mathrm{m}} \times \boldsymbol{s}_2^{\mathrm{m}} & \boldsymbol{r}_{O0}^{\mathrm{m}} \times \boldsymbol{s}_3^{\mathrm{m}} & \boldsymbol{s}_1^{\mathrm{w}} & \boldsymbol{s}_2^{\mathrm{w}} \end{bmatrix} [v_{\mathrm{d}}^{\mathrm{m}}, v_{\theta 1}^{\mathrm{m}}, v_{\theta 2}^{\mathrm{m}}, v_{\mathrm{d1}}^{\mathrm{w}}, v_{\mathrm{d2}}^{\mathrm{w}}]^{\mathrm{T}} \\ &= \boldsymbol{J}_{\mathrm{wp\text{-}Tool}}[v_{\mathrm{d}}^{\mathrm{m}}, v_{\theta 1}^{\mathrm{m}}, v_{\theta 2}^{\mathrm{m}}, v_{\mathrm{d1}}^{\mathrm{w}}, v_{\mathrm{d2}}^{\mathrm{w}}]^{\mathrm{T}} \end{aligned} \tag{48}$$

A 5-axis hybrid machine tool will occur singularities, when rank($\boldsymbol{J}_{\mathrm{wp\text{-}Tool}}$)<5. The singularity of a 5-axis hybrid machine tool can be concluded as followings:

1) The 1T2R parallel mechanism or the X-Y sliding gantry module suffers singularity.

2) The translational axis of the parallel mechanism is parallel to that of the X or the Y sliding gantry. Under this configuration, the hybrid machine tool will possess two identical translational DOF. This means the hybrid machine tool lose one linearly independent translational DOF to change the position of tool.

3) The rotational axis of the parallel mechanism is coincided with the tool axis. Under this configuration, the corresponding rotational DOF will lose the capacity to adjust the posture of tool.

According to the features of the constructed hybrid machine tool as shown in Fig. 5, one may easily find that: (1) the serial module is composed of two orthogonal sliding gantries, whose translational axes are always perpendicular to the translational axis of the parallel module; (2) the tool axis is perpendicular to the two rotational axes of the parallel module. Therefore, the constructed hybrid machine tool may occur singularity, only when the RAVASH is under singular configuration.

Measured in the frame of $O\text{-}xyz$, the linear velocities of $\boldsymbol{v}_{Ai}$ and $\boldsymbol{v}_{Ci}$ for A_i and C_i can be given as

$$\begin{cases} \boldsymbol{v}_{Ai} = \boldsymbol{v}_{O0} + \boldsymbol{\omega}_{\text{out}} \times \boldsymbol{r}_{ai},\ \boldsymbol{v}_{Ci} = d_i' \boldsymbol{v}_{di} \\ \boldsymbol{v}_{Aj} = \boldsymbol{v}_{O0} + \boldsymbol{\omega}_{\text{R}} \times \boldsymbol{r}_{aj} + \boldsymbol{\omega}_{\text{out}} \times \boldsymbol{r}_{aj},\ \boldsymbol{v}_{Cj} = d_j' \boldsymbol{v}_{dj} \end{cases} \quad (i\text{=1, 2; } j\text{=3, 4}) \tag{49}$$

where $\boldsymbol{v}_{O0}$ represents the linear velocity of O_0; $\boldsymbol{\omega}_{\text{out}}$ denotes the angular velocity of MP1; $\boldsymbol{\omega}_{\text{R}}$ denotes the relative angular velocity of MP2 with respect to MP1.

Since the length l of limb body is constant, it leads to

$$(\boldsymbol{v}_{Ai} - \boldsymbol{v}_{Ci})\boldsymbol{s}_{li} = 0 \quad (i\text{=1-4}) \tag{50}$$

where $\boldsymbol{s}_{li}$ is a unit vector pointing form C_i to A_i.

By substituting Eq. (49) into Eq. (50), one may obtain

$$\begin{cases} d_i' = \dfrac{\boldsymbol{s}_{li}}{\boldsymbol{v}_{di}\boldsymbol{s}_{li}} \boldsymbol{v}_{O0} + \dfrac{\boldsymbol{r}_{ai} \times \boldsymbol{s}_{li}}{\boldsymbol{v}_{di}\boldsymbol{s}_{li}} \boldsymbol{\omega}_{\text{out}} \\ d_j' = \dfrac{\boldsymbol{s}_{lj}}{\boldsymbol{v}_{dj}\boldsymbol{s}_{lj}} \boldsymbol{v}_{O0} + \dfrac{\boldsymbol{r}_{aj} \times \boldsymbol{s}_{lj} + Q_j \boldsymbol{r}_{aj} \times \boldsymbol{s}_{j,2}}{\boldsymbol{v}_{dj}\boldsymbol{s}_{lj}} \boldsymbol{\omega}_{\text{out}} \end{cases} \quad (i\text{=1, 2; } j\text{=3, 4}) \tag{51}$$

where $Q_j = -\dfrac{(\boldsymbol{r}_{aj} \times \boldsymbol{s}_{lj})\boldsymbol{s}_{\text{R}}}{(\boldsymbol{r}_{aj} \times \boldsymbol{s}_{j,2})\boldsymbol{s}_{\text{R}}}$ (j=3, 4).

Eq. (51) can be rewritten in the matrix form as

$$\begin{bmatrix} d_1' & d_2' & d_3' & d_4' \end{bmatrix}^{\text{T}} = \boldsymbol{J}_a \begin{bmatrix} \boldsymbol{v}_{O0} \\ \boldsymbol{\omega}_{\text{out}} \end{bmatrix} \tag{52}$$

where $\boldsymbol{J}_a$ denotes the Jacobian matrix of actuations

$$\boldsymbol{J}_a = \begin{bmatrix} (\dfrac{\boldsymbol{s}_{l1}}{\boldsymbol{v}_{d1}\boldsymbol{s}_{l1}})^{\text{T}} & \dfrac{(\boldsymbol{r}_{a1} \times \boldsymbol{s}_{l1})^{\text{T}}}{\boldsymbol{v}_{d1}\boldsymbol{s}_{l1}} \\ (\dfrac{\boldsymbol{s}_{l2}}{\boldsymbol{v}_{d2}\boldsymbol{s}_{l2}})^{\text{T}} & \dfrac{(\boldsymbol{r}_{a2} \times \boldsymbol{s}_{l2})^{\text{T}}}{\boldsymbol{v}_{d2}\boldsymbol{s}_{l2}} \\ (\dfrac{\boldsymbol{s}_{l3}}{\boldsymbol{v}_{d3}\boldsymbol{s}_{l3}})^{\text{T}} & \dfrac{(\boldsymbol{r}_{a3} \times \boldsymbol{s}_{l3} + Q_3 \boldsymbol{r}_{a3} \times \boldsymbol{s}_{3,2})^{\text{T}}}{\boldsymbol{v}_{d3}\boldsymbol{s}_{l2}} \\ (\dfrac{\boldsymbol{s}_{l4}}{\boldsymbol{v}_{d4}\boldsymbol{s}_{l4}})^{\text{T}} & \dfrac{(\boldsymbol{r}_{a4} \times \boldsymbol{s}_{l4} + Q_4 \boldsymbol{r}_{a4} \times \boldsymbol{s}_{4,2})^{\text{T}}}{\boldsymbol{v}_{d4}\boldsymbol{s}_{l4}} \end{bmatrix} \tag{53}$$

By taking inner product on both sides of Eq. (49) with the vectors of $\boldsymbol{s}_{i,2}$, $\boldsymbol{s}_{i,2}\times\boldsymbol{s}_{i,4}$, and $\boldsymbol{s}_{j,2}$ (i=1, 2; j=3, 4) respectively, one may obtain

$$\begin{cases} \boldsymbol{s}_{i,2}\boldsymbol{v}_{O0} + \boldsymbol{r}_{ai} \times \boldsymbol{s}_{i,2}\boldsymbol{\omega}_{\text{out}} = 0 \\ (\boldsymbol{s}_{i,2} \times \boldsymbol{s}_{i,4}) \times \boldsymbol{\omega}_{\text{out}} = 0 \end{cases} \quad (i\text{=1, 2}) \tag{54}$$

$$\boldsymbol{s}_{j,2}\boldsymbol{v}_{O0} + \boldsymbol{r}_{aj} \times \boldsymbol{s}_{j,2}\boldsymbol{\omega}_{\text{out}} = 0 \quad (j\text{=3, 4}) \tag{55}$$

Rewriting Eq. (54) and Eq. (55) into the matrix form, one may obtain

$$\boldsymbol{J}_{c0} \begin{bmatrix} \boldsymbol{v}_{O0} \\ \boldsymbol{\omega}_{\text{out}} \end{bmatrix} = \boldsymbol{0}_{6\times1} \tag{56}$$

where $\boldsymbol{J}_{c0}$ denote the Jacobian matrix of constraints, and can be further expressed as

$$\boldsymbol{J}_{c0}=\begin{bmatrix}\boldsymbol{s}_{1,2}^{\mathrm{T}} & (\boldsymbol{r}_{a1}\times\boldsymbol{s}_{1,2})^{\mathrm{T}}\\ \boldsymbol{0}_{3\times1}^{\mathrm{T}} & (\boldsymbol{s}_{1,2}\times\boldsymbol{s}_{1,4})^{\mathrm{T}}\\ \boldsymbol{s}_{2,2}^{\mathrm{T}} & (\boldsymbol{r}_{a2}\times\boldsymbol{s}_{2,2})^{\mathrm{T}}\\ \boldsymbol{0}_{3\times1}^{\mathrm{T}} & (\boldsymbol{s}_{2,2}\times\boldsymbol{s}_{2,4})^{\mathrm{T}}\\ \boldsymbol{s}_{3,2}^{\mathrm{T}} & (\boldsymbol{r}_{O0}\times\boldsymbol{s}_{3,2})^{\mathrm{T}}\\ \boldsymbol{s}_{4,2}^{\mathrm{T}} & (\boldsymbol{r}_{O0}\times\boldsymbol{s}_{4,2})^{\mathrm{T}}\end{bmatrix} \tag{57}$$

According to the aforementioned geometrical constraints of the RAVASH, the maximal linearly independent array of $\boldsymbol{J}_{c0}$ may be derived as

$$\boldsymbol{J}_{c}=\begin{bmatrix}\boldsymbol{s}_{i,2}^{\mathrm{T}} & (\boldsymbol{r}_{ai}\times\boldsymbol{s}_{i,2})^{\mathrm{T}}\\ \boldsymbol{0}_{3\times1}^{\mathrm{T}} & (\boldsymbol{s}_{i,2}\times\boldsymbol{s}_{i,4})^{\mathrm{T}}\\ \boldsymbol{s}_{j,2}^{\mathrm{T}} & (\boldsymbol{r}_{O0}\times\boldsymbol{s}_{j,2})^{\mathrm{T}}\end{bmatrix}\quad (i=1,\ 2;\ j=3,\ 4) \tag{58}$$

Therefore, the overall Jacobin matrix $\boldsymbol{J}$ can be given by

$$\boldsymbol{J}=\begin{bmatrix}\boldsymbol{J}_{a}\\ \boldsymbol{J}_{c}\end{bmatrix} \tag{59}$$

According to Jacobin matrix shown in Eq. (59), one may analyze the singularity of the RAVASH as the follows.

(1) Constraint singularity analysis

Since $\boldsymbol{s}_{i,2}\perp\boldsymbol{s}_{i,4}$ and $\boldsymbol{s}_{i,2}\perp\boldsymbol{s}_{j,2}$ (i= 1, 2; j= 3, 4), it leads to

$$\boldsymbol{s}_{i,2}\times\boldsymbol{s}_{i,4}\neq 0,\quad \boldsymbol{s}_{i,2}\neq\boldsymbol{s}_{j,2} \tag{60}$$

Thus, the rank of $\boldsymbol{J}_c$ is always equal to 3, i.e. rank($\boldsymbol{J}_c$)=6-f. Herein, rank(*) means the rank function which provides an estimated number of linearly independent rows of a matrix. f=3 is the number of DOFs of the RAVASH. This indicates that there is no constraint singularity in RAVASH.

(2) Architecture singularity analysis

The proposed RAVASH will occur architecture singularities, when rank($\boldsymbol{J}_a$)≤ f or rank($\boldsymbol{J}$) ≤6. Fig. 8 shows four typical singular configurations of the proposed RAPM.

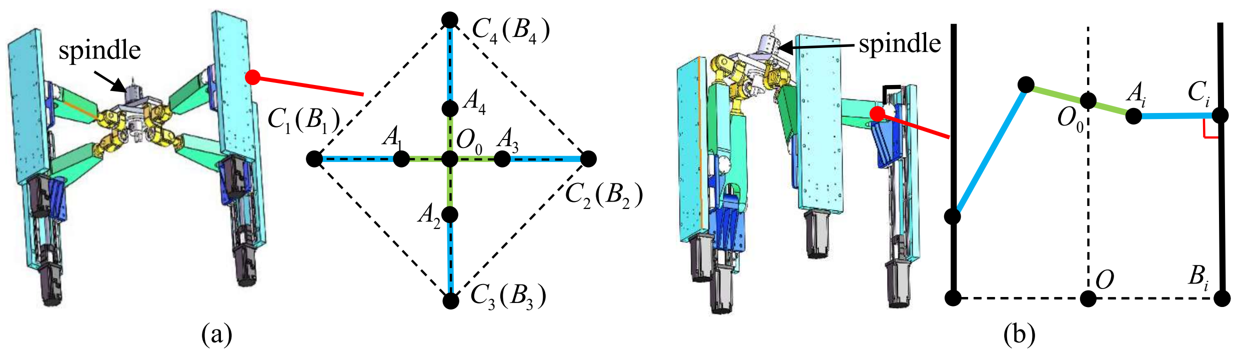

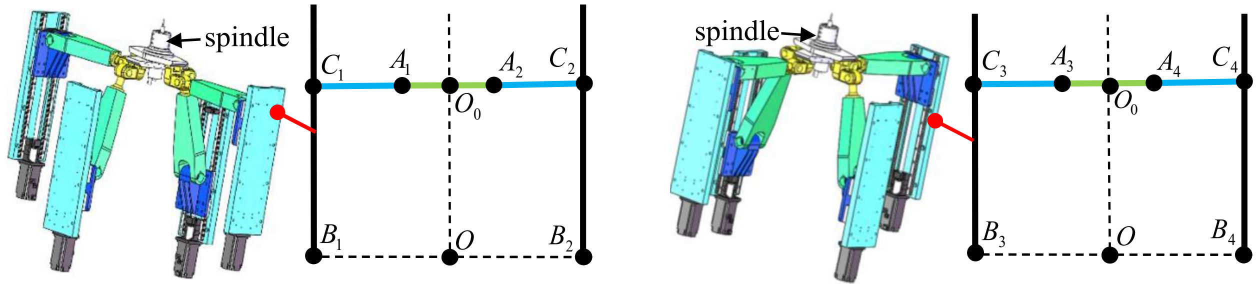

(c) (d)

Fig. 8 Four singular configurations of the proposed RAVASH

Case 1: as shown in Fig. 8 (a), when C_1A_1 is coincident with C_2A_2 and C_3A_3 is coincident with C_4A_4, it leads to

$$\boldsymbol{s}_{l1}=\boldsymbol{s}_{l2},\ \ \boldsymbol{v}_{d1}\boldsymbol{s}_{l1}=\boldsymbol{v}_{d2}\boldsymbol{s}_{l2},\ \ \boldsymbol{r}_{a1}\times\boldsymbol{s}_{l1}=\boldsymbol{r}_{a2}\times\boldsymbol{s}_{l2},\ \ \boldsymbol{s}_{l3}=\boldsymbol{s}_{l4},\ \ \boldsymbol{v}_{d3}\boldsymbol{s}_{l3}=\boldsymbol{v}_{d4}\boldsymbol{s}_{l4},\ \ \boldsymbol{r}_{a3}\times\boldsymbol{s}_{l3}=\boldsymbol{r}_{a4}\times\boldsymbol{s}_{l4},\ \ Q_3=Q_4=0 \tag{61}$$

By substituting Eq. (61) into Eq. (53), one may obtain

$$\boldsymbol{J}_a(1)=\boldsymbol{J}_a(2),\ \ \boldsymbol{J}_a(3)=\boldsymbol{J}_a(4) \tag{62}$$

where $\boldsymbol{J}_a(i)$ (i=1-4) denotes the i^{th} row of the $\boldsymbol{J}_a$ matrix.

Thus,

$$\text{rank}(\boldsymbol{J}_a)=2<f \tag{63}$$

Case 2: as shown in Fig. 8 (b), when the limb body is perpendicular to the prismatic joint in the i^{th} chain, it leads to

$$\boldsymbol{v}_{di}\boldsymbol{s}_{li}=0 \tag{64}$$

In such a circumstance, denominators in the $\boldsymbol{J}_a$ matrix of Eq. (53) do not make sense.

Case 3: as shown in Fig. 8 (c), when C_1A_1 is coincident with C_2A_2 and parallel to $\boldsymbol{s}_{j,2}$ (j=3, 4), it leads to

$$\boldsymbol{s}_{l1}=\boldsymbol{s}_{l2}=\boldsymbol{s}_{j,2}^{\text{T}},\ \ \boldsymbol{v}_{d1}\boldsymbol{s}_{l1}=\boldsymbol{v}_{d2}\boldsymbol{s}_{l2},\ \ \boldsymbol{r}_{a1}\times\boldsymbol{s}_{l1}=\boldsymbol{r}_{a2}\times\boldsymbol{s}_{l2}=\boldsymbol{r}_{O0}\times\boldsymbol{s}_{j,2}\ \ (j=3,\ 4) \tag{65}$$

By substituting Eq. (65) into Eq. (53), one may obtain

$$\boldsymbol{J}_a(1)=\boldsymbol{J}_a(2)=\frac{1}{\boldsymbol{v}_{d1}\boldsymbol{s}_{l1}}\boldsymbol{J}_c(3) \tag{66}$$

Thus,

$$\text{rank}(\boldsymbol{J})=5<6 \tag{67}$$

Case 4: as shown in Fig. 8 (d), when C_3A_3 is coincident with C_4A_4 and parallel to $\boldsymbol{s}_{i,2}$ (i=1, 2), it leads to

$$\boldsymbol{s}_{l3}=\boldsymbol{s}_{l4}=\boldsymbol{s}_{i,2},\ \ \boldsymbol{v}_{d3}\boldsymbol{s}_{l3}=\boldsymbol{v}_{d4}\boldsymbol{s}_{l4},\ \ \boldsymbol{r}_{a3}\times\boldsymbol{s}_{l3}=\boldsymbol{r}_{a4}\times\boldsymbol{s}_{l4}=\boldsymbol{r}_{O0}\times\boldsymbol{s}_{i,2},\ \ Q_3=Q_4=0\ \ (i=1,\ 2) \tag{68}$$

By substituting Eq. (68) into Eq. (53), one may obtain

$$\boldsymbol{J}_a(3)=\boldsymbol{J}_a(4)=\frac{1}{\boldsymbol{v}_{d3}\boldsymbol{s}_{l3}}\boldsymbol{J}_c(1) \tag{69}$$

Thus,

$$\text{rank}(\boldsymbol{J})=5<6 \tag{70}$$

From the above singularity analysis, the RAVASH as well as the constructed hybrid machine tool are free of constraint singularity but may occur architecture singularity under the above four configurations.

4. Hierarchical fabrication and orientation workspace prediction

4.1. Hierarchical fabrication of a hybrid machine tool

In this subsection, a scaled-down laboratory prototype is fabricated by adopting a hierarchical design methodology proposed by the authors [32]. The fabricated prototype is demonstrated in Fig. 9.

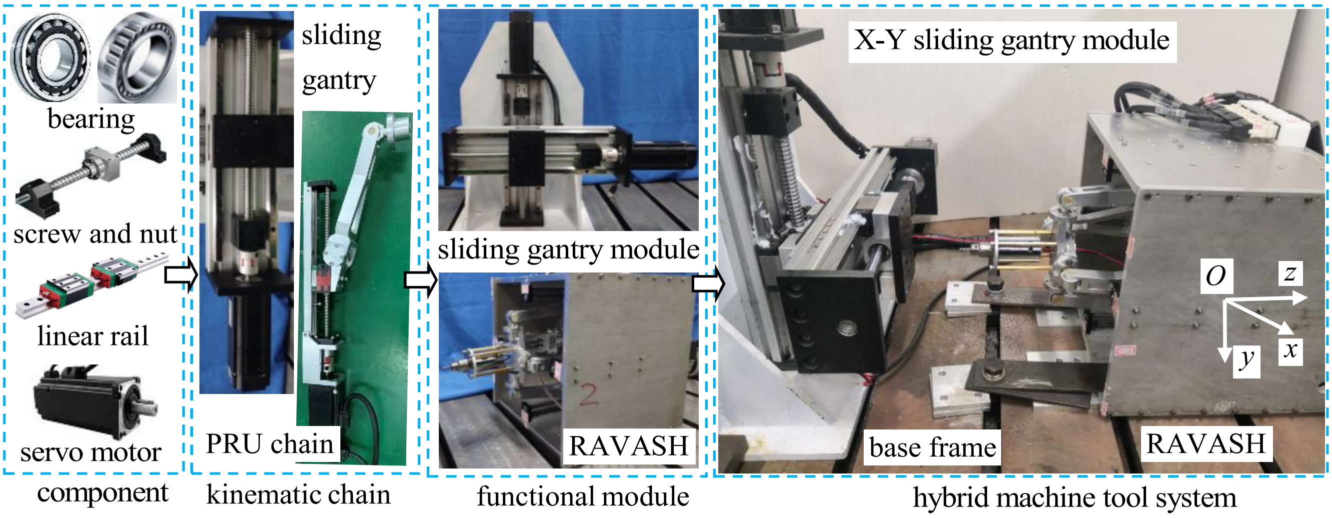

Fig. 9 Hierarchical fabrication of the proposed 5-axis hybrid machine tool

As shown in Fig. 9, the hybrid machine tool is hierarchically fabricated at four different levels, i.e., the component, the kinematic chain, the functional module and the system. To be specific, a servo motor, a lead-screw assemblage, a revolute joint and a universal joint construct an individual PRU kinematic chain. Two orthogonal sliding gantries form an X-Y sliding gantry module. Four PRU kinematic chains are symmetrically arranged to construct the RAVASH. The RAVASH and the X-Y sliding gantry module are assembled in a horizontal-type arrangement to construct the hybrid machine tool.

For clarity, Table 2 gives basic dimensional parameters of the laboratory prototype.

Table 2 Dimensional parameters of the laboratory prototype

θ_{Rmin}	θ_{Rmax}	$\theta_{i,\mathrm{Rmin}}$	$\theta_{i,\mathrm{Rmax}}$	$\theta_{i,\mathrm{1Umin}}$	$\theta_{i,\mathrm{1Umax}}$	$\theta_{i,\mathrm{2Umin}}$	$\theta_{i,\mathrm{2Umax}}$
60°	120°	88°	165°	54°	180°	0°	180°
$d_{i,\mathrm{min}}$	$d_{i,\mathrm{max}}$	r_a	r_b	l	d_{P}	$d_{\mathrm{XY,min}}$	$d_{\mathrm{XY,max}}$
140 mm	650 mm	256 mm	259 mm	390 mm	300.5 mm	-100 mm	100 mm

Herein, θ_{Rmin} and θ_{Rmax} are the minimal and the maximal rotating angles of the revolute joint connecting MP1 and MP2; $\theta_{i,\mathrm{Rmin}}$ and $\theta_{i,\mathrm{Rmax}}$ denote the minimal and the maximal rotating angles of the revolute joint in the PRU kinematic chain; $\theta_{i,\mathrm{1Umin}}$ ($\theta_{i,\mathrm{1Umax}}$) and $\theta_{i,\mathrm{2Umin}}$ ($\theta_{i,\mathrm{2Umax}}$) denote the minimal rotating angle (the maximal rotating angle) of the two rotational axes of the universal joint; $d_{i,\mathrm{min}}$ and $d_{i,\mathrm{max}}$ represent the allowable minimal and the maximal displacements of the i^{th} actuator. $d_{\mathrm{XY,min}}$ and $d_{\mathrm{XY,max}}$ are the allowable minimal and the allowable maximal displacements of the X/ Y sliding gantries.

Based on above laboratory prototype, a numerical control (NC) system is developed as shown in Fig. 10.

Fig. 10 NC system of the developed 5-axis hybrid machine tool

As shown in Fig. 10, the NC system mainly contains of a host computer, a motion controller, six servo drivers, a transducer, and a human machine interface (HMI) system. The host computer, the motion controller, and the servo drivers communicate with each other through the Ethernet and the I/O interface.

By integrating the fabricated laboratory prototype with the self-developed NC system, a 5-axis hybrid machine tool system is constructed as depicted in Fig. 11.

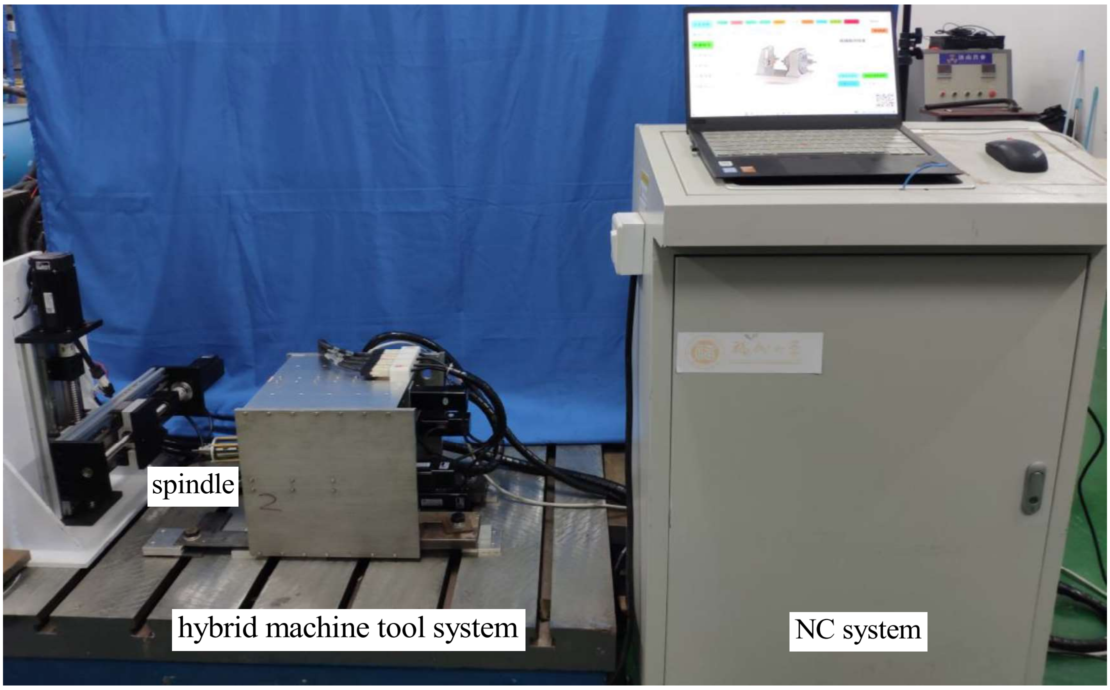

Fig. 11 An electromechanical system of the hybrid machine tool

Table 3 gives some technical specifications of the developed electromechanical system.

Table 3 Some technical specifications of the laboratory prototype

Object	Parameter	Value
host computer	operating system	Windows 10
	communication model	Ethernet
motion controller	interpolation	6 axes
	programming language	C#
servo motor	nominal voltage	220 v
	rated power (in RAVASH)	100 w
	rated power (in sliding gantry)	400 w
worktable	maximum dimension of workpiece	100 mm×100 mm×50 mm
spindle	type	DC motor
	rated power	90w or 150 w
	maximum speed	3000 r/min
cutter	diameter	2 mm ~5 mm
	length	35 mm ~75 mm
machine tool	overall dimensions	1.2 m×0.5 m×2.1 m
	weight	92 kg
	input voltage	220 V

4.2. Orientation workspace prediction

The orientation capacity is one of the most important performances for 5-axis machine tools. Since the two rotational DOFs of the proposed hybrid machine tool is realized by the parallel functional module, the following will explore the orientation workspace of the RAVASH.

To examine the orientation capability of the RAVASH, a slice-partition searching algorithm [25, 32] is adopted to identify the orientation workspace. Its basic idea can be described as follow:

Step 1: The potential workspace of the RAVASH is predicted with the aid of SolidWorks and 'sliced' into a series of work planes with an increment of Δz=5mm. Each work plane is further meshed into discrete grids and notes with increment coordinates of ψ and θ ($\Delta\theta$=2° and $\Delta\psi$=2°). Herein, each note is regarded as a potential reachable posture.

Step 2: The rotational angles of passive joints and the displacements of actuated joints are calculated through the inverse kinematic formulations at the current posture. The allowable angles of passive joints and the extreme displacements of actuated joints are employed to judge whether a posture is a reachable posture or not.

Step3: Above steps are repeated with increment of ψ, θ and z, respectively. During the process, all the reachable postures are recorded to form the reachable orientation workspace of the RAVASH.

For clarity, the above workspace prediction process is depicted in a flowchart as shown in Fig. 12.

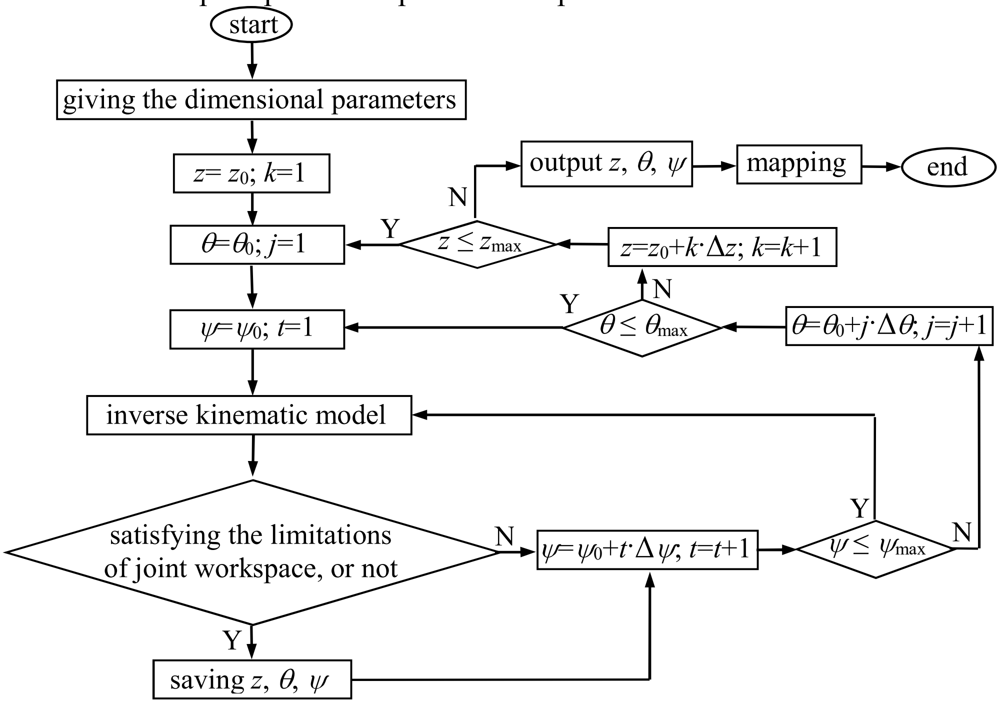

Fig. 12 Flowchart of orientation workspace search

After using above searching algorithm, the orientation workspace of the 2PRU-(2PRU)R RAPM can be calculated and demonstrated in Fig. 13.

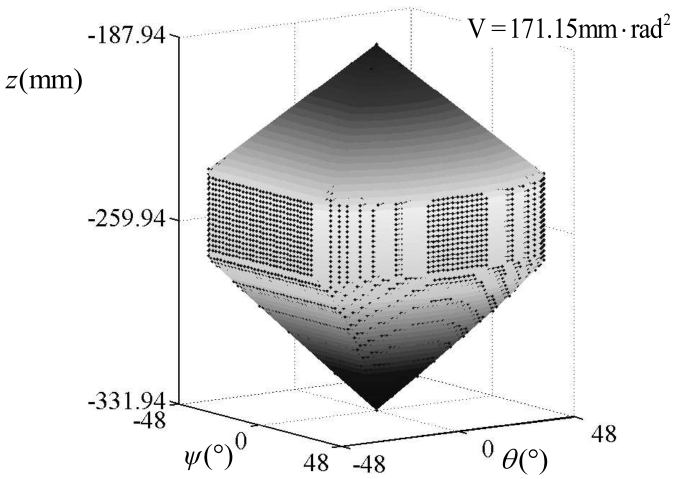

Fig. 13 The orientation workspace of the RAVASH

As shown in Fig. 13, the orientation workspace of the proposed RAVASH is a symmetric polyhedron, whose volume is 171.15 mm·rad^2. Based on the previous velocity solution, the Jacobian matrix ($\boldsymbol{J}$, $\boldsymbol{J}_a$, $\boldsymbol{J}_c$)

and their rank can also be calculated during the workspace prediction. The results show that the rank of $\boldsymbol{J}$ is always equivalent to 6, the rank of $\boldsymbol{J}_a$ is always equivalent to 4 and the rank of $\boldsymbol{J}_c$ is always equivalent to 3. This indicates the fabricated RAVASH is free of constraint singularity as well as architecture singularity throughout its workspace.

To further clarify the features of the orientation workspace, Fig. 14 illustrates the projected cross-sections of z=-260 mm, ψ=0° and θ=0°.

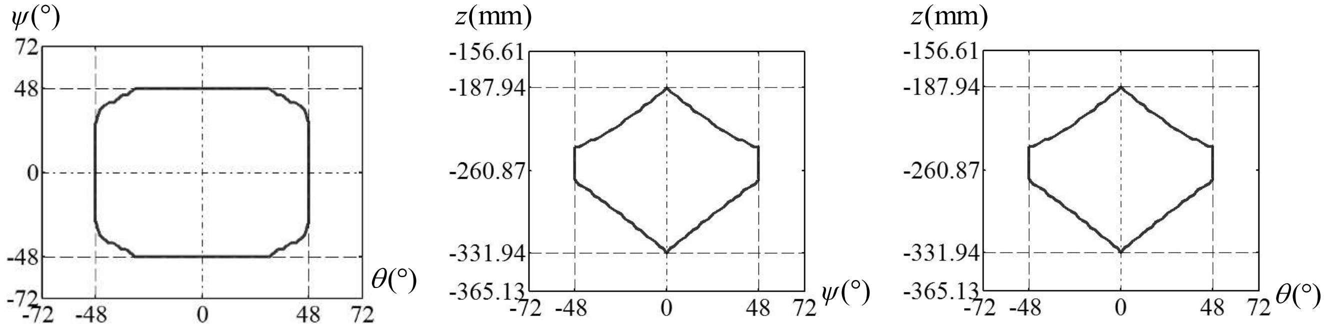

(a) Cross-section of z=-260 mm (b) Cross-section of θ=0° (c) Cross-section of ψ=0°

Fig. 14 The cross-sections of the orientation workspace

It can be observed from Fig. 14 (a) that the orientation workspace of the proposed RAVASH is symmetric about the plane of ψ=0° and θ=0°. This is coincident with the fact that limb 1 limb 2, limb 3 and limb 4 are symmetrical arranged. Furthermore, the boundaries of the orientation angles ψ and θ are all within in the interval of [-48°, 48°]. This indicates that the proposed RAVASH can achieve 'stronger' orientation capacity compared with the Exechon parallel module ([-36°, 36°], [47]) and the Sprint Z3 head ([-45°, 45°], [4]) at approximate geometric levels. Meanwhile, Fig. 14 (b) and Fig. 14 (c) show that the available stroke of the platform along z axis is within in the interval of [-331.94 mm, -187.94 mm] while ψ=0° and θ=0°.

4.3. Discussion

Based on the above investigations, the potential advantages of the proposed 1T2R RAPM may be concluded as follows:

(1) From the aspect of topological architecture, the proposed 1T2R 2PRU-(2PRU)R RAPM only consists of PRU-type lower-mobility kinematic chains. The four symmetrically arranged PRU limb is benefit for improving performance isotropy of the proposed RAPM. Without spherical joint used in its chain system, it may be easier to achieve desirable stiffness and accuracy performances as indicated by previous references [40-42]. In addition, the characteristic of only one over-constraint in the direction of each constraint, not only helps to enhance the overall stiffness of the constructed RAPM, but also helps to relief internal forces. These features inherently help to eliminate or mitigate the three critical drawbacks of traditional 1T2R RAPMs as described in Section 1.

(2) According to the kinematic analysis, the proposed 1T2R RAPM has symmetrical orientation workspace about the plane of ψ=0° and θ=0° and 'strong' rotational capability with ψ and θ ranging from -48° to 48°. Throughout its reachable orientation workspace, it is free of constraint singularity as well as architecture singularity. Besides, it possesses two continuous rotational axes and does not generate parasitic motion. This may indicate that it has a 'better' kinematic performance and is therefore easy to implement trajectory planning, kinematic calibration and motion control [23, 39, 48].

5. Experimental tests

In this section, a set of motion experiments and machining tests are accomplished on the laboratory prototype to further verify the aforementioned mobility, the orientation workspace prediction and the 5-axis machining capability.

5.1. Mobility validation

To graphically demonstrate the mobility of the proposed parallel mechanism, Fig. 15 presents four typical configurations of the developed laboratory prototype.

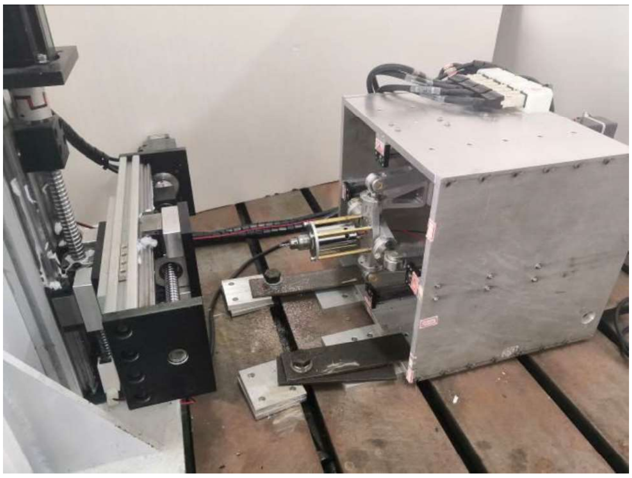

(a) Home position

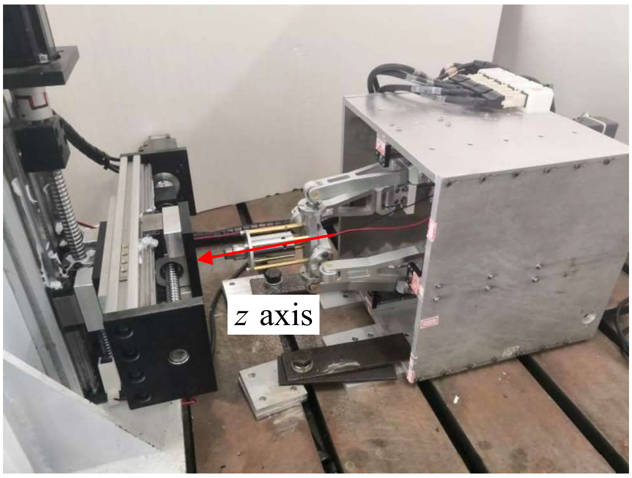

(b) Translating alone z axis

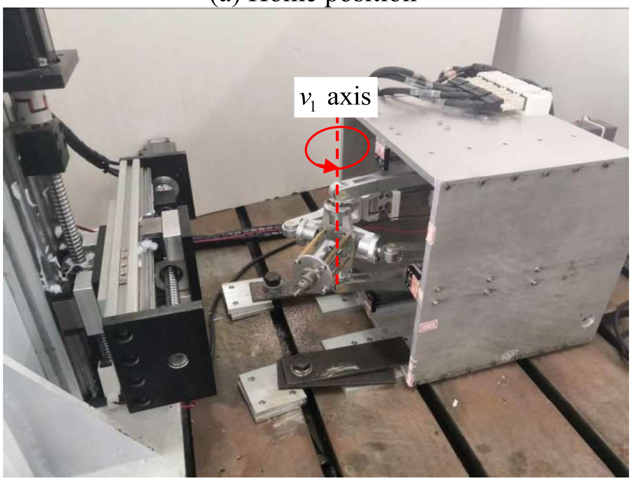

(c) Rotating about v_1 axis

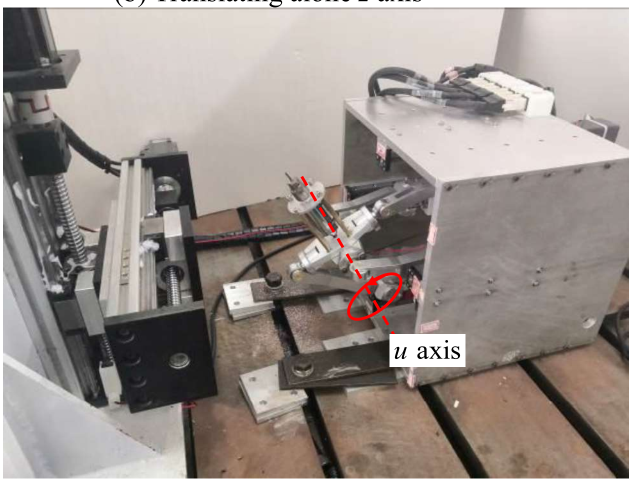

(d) Rotating about u axis

Fig. 15 Four typical configurations of the laboratory prototype

Fig. 15 (a) illustrates the home position of the laboratory prototype, where the four identical PRU kinematic chains locate at the extreme position and the dual platform is parallel to □$B_1B_2B_3B_4$. As can be seen from Fig. 15 (b), when the four PRU kinematic chains are driven simultaneously by servo motors, the platform demonstrates a configuration of translating along z axis. As shown in Fig. 15 (c), when limb 1 and limb 3 undergo opposite inputs, the platform demonstrates a configuration of rotating about v_1 axis. As shown in Fig. 15 (d), when limb 2 and limb 4 undergo opposite inputs, the platform demonstrates a configuration of rotating about u axis. Obviously, the proposed RAVASH possesses 1T2R motion capabilities, which further proves the synthesized RAPM can fulfill required 1T2R motions. Obviously, when the X and Y sliding gantries are actuated to adjust the position of the worktable, the spindle has a relative three translational and two rotational motions with respect to the workpiece.

5.2. Orientation workspace validation

The maximum/minimum rotational angle is an important index to describe the boundary of reachable orientation workspace and can be used to evaluate the orientation capacity of a 5-axis hybrid machine tool. The two postures with maximum θ and ψ are chosen as experimental examples to demonstrate the orientation ability of the developed prototype. Fig. 16 illustrates the two extreme configurations of the prototype.

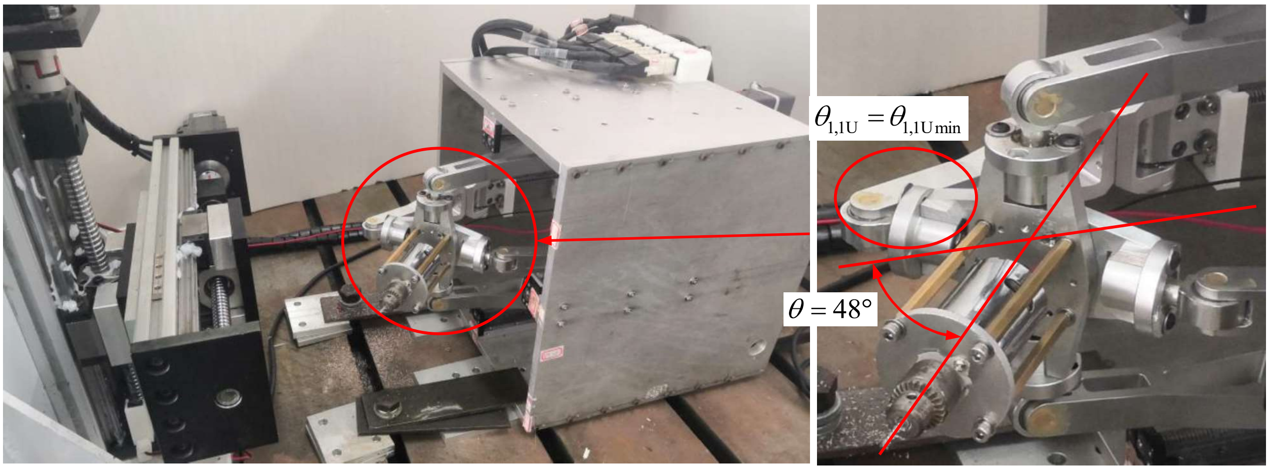

(a) ψ=0° and θ=48°

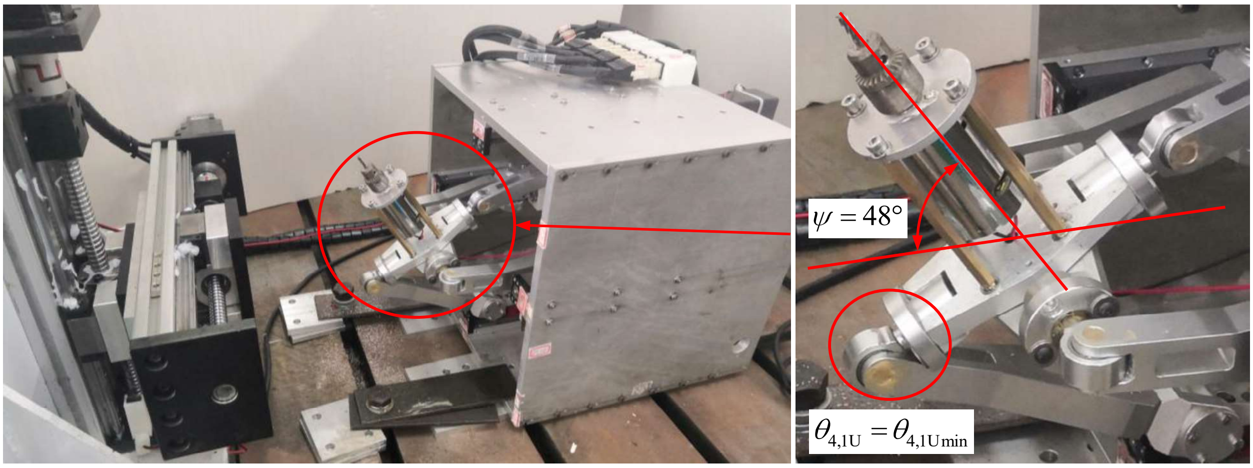

(b) ψ=48° and θ=0°

Fig. 16 Two extreme configurations of the laboratory prototype

Fig. 16 (a) shows an extreme configuration θ=48° of the laboratory prototype when $\theta_{1,1U}$=58°. Under this configuration, the four actuators' displacements (d_1=37.81 mm, d_2=151.51 mm, d_3=89.46 mm, d_4=89.46 mm) can be calculated by the pulse feedback from the encoder. According to Eq. (31), Eq. (34), and Eq. (36), the platform's posture parameters can be obtained as θ=48°, ψ=0°, and z=-241.4mm. Fig. 16 (b) shows another extreme configuration ψ=48° of the laboratory prototype when $\theta_{4,1U}$=58°. Similarly, the platform's posture parameters can be solved as θ=0°, ψ=48°, and z=-241.4 mm with d_1=89.46 mm, d_2=89.46 mm, d_3=37.81 mm, d_4=151.51 mm. Obviously, these experimental results are well consistent with the theoretical predicted results, indicating the correctness of orientation workspace prediction.

5.3. 5-axis machining tests

To verify the feasibility and the engineering potential of the proposed 5-axis hybrid machine tool, a set of machining tests for S-shaped workpiece (ISO 10791-7), spherical crown workpiece and polyhedral workpiece are performed on the laboratory prototype. For clarity, the operating steps of the machining test are summarized and depicted in Fig. 17.

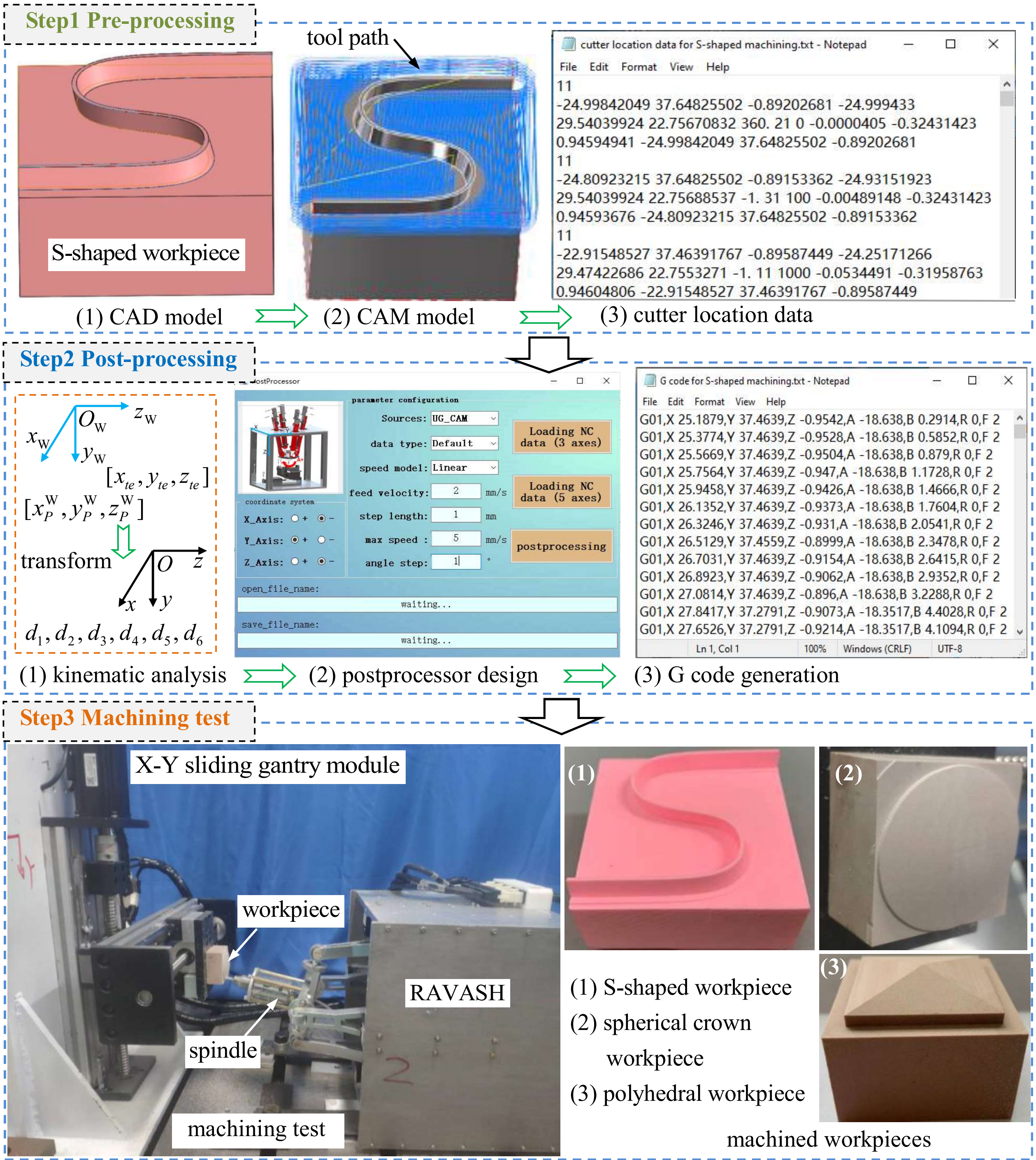

Fig. 17 Operations of 5-axis machining test

As depicted in Fig. 18, the 5-axis machining operation can be divided into three stages, i.e. pre-processing, post-processing and machining test. In the stage of pre-processing, a conceptual workpiece is developed by CAD software such as SolidWorks. The CAD model is transformed into a CAM model to generate the tool path and the cutter location (CL) data. During the post-processing stage, positions and velocities of actuators at each cutter location are calculated through the aforementioned kinematic analysis. On this base, the CL data is converted into G codes to provide necessary information for the control of servo motors and spindle. During the machining test stage, the G codes are uploaded into the HMI system to produce motion commands to drive the six servo motors and the spindle simultaneously. Meanwhile, the HMI system collects the feedback information from servo drivers and displays the machine system's status on the screen.

For clarity, Table 4 shows the basic experiment parameters.

Table 4 Basic experiment parameters of a machining test

Object	Parameter	Value
cutter	radius	2 mm
	overhang length of cutter	28.5mm
	type	side milling cutter
blank	length×width×height	50 mm×50 mm ×25 mm
	workblank	man-made epoxy tooling board
machining parameters	average feed rate	2 mm/s
	maximum axial cutting depth	1 mm
	maximum radial cutting depth	2 mm
	milling operation	down milling

In addition, a set of surface roughness test for the machined S-shape workpiece is carried out as shown in Fig. 18.

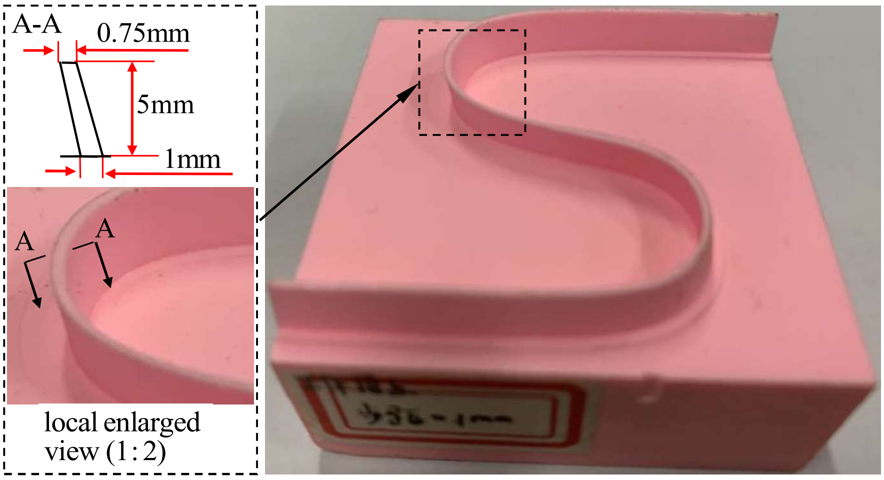

(a) The machined S-shape workpiece

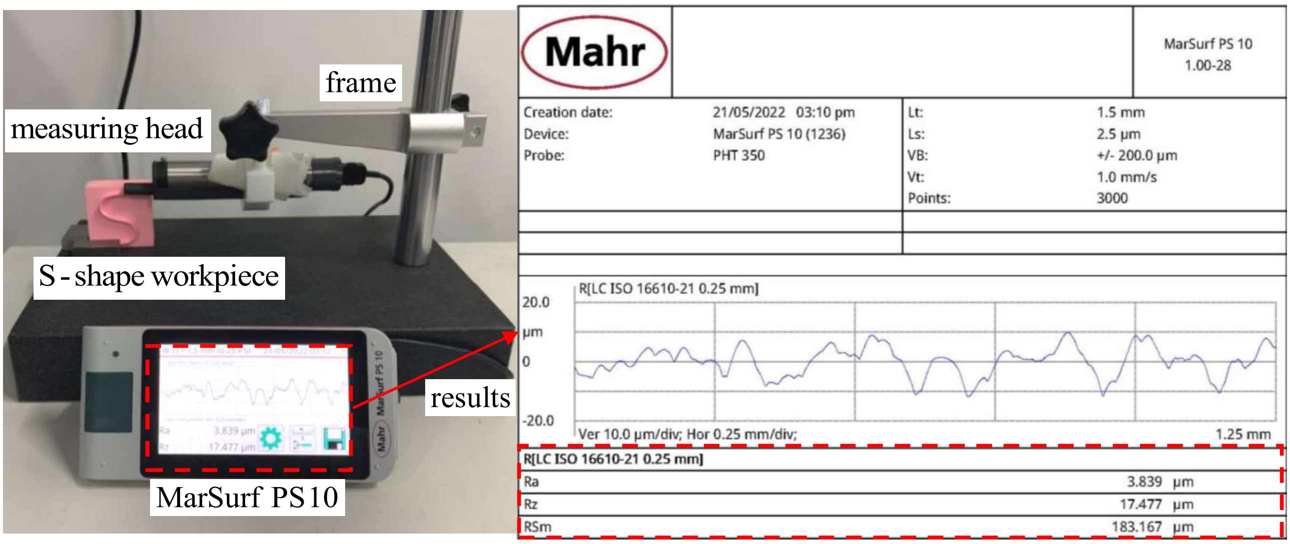

(b) A set of Surface roughness test

Fig. 18 Surface roughness test of the machined S-shape workpiece

As shown in Fig. 18 (a), the machined S-shape workpiece is a thin-walled part. A poor machining accuracy will lead to obvious overcut and may destroy the S-shape especially around the corner. As can be seen from Fig. 18 (a), there is no obvious overcut occurred throughout the overall S-shape surface. This indicates that the machined S-shaped workpiece may have a good machining consistency. As shown in Fig. 18 (b), the roughness test results show that the values of roughness indices Ra and Rz for the machined S-shaped workpiece are 3.839μm and 17.477μm. This indicates that the machined S-shaped workpiece have smooth surfaces. According to the machining test and roughness test, the laboratory prototype of the proposed hybrid machine tool may possess 5-axis machining capability, which can be used for machining structure component with complex geometries.

6. Conclusions

Based on the investigations conducted in this paper, the following conclusions can be drawn:

1) A screw theory based type synthesis is proposed to invent a family of 1T2R RAPMs through solid mathematical derivation. From the point of view of reducing motion inertia, a 2PRU-(2PRU)R RAPM with symmetrical structure is selected and developed as a 3-DOF spindle head named RAVASH.
2) By incorporating the proposed RAVASH with two orthogonal sliding gantries, a novel 5-axis hybrid machine tool is constructed. The inverse/ forward position and the singularity of the constructed hybrid machine tool are investigated to reveal its fundamental kinematic properties. The results indicate that the RAVASH as well as the constructed hybrid machine tool is free of constraint singularity. However, they may exist four kinds of architecture singularity.
3) A laboratory prototype of the proposed hybrid machine tool is hierarchically fabricated and an open-architecture NC system with a HMI system is developed. The orientation workspace of the developed prototype are predicted and experimentally tested to manifest the developed prototype possessing a 'strong' orientation capacity with ψ and θ ranging from -48° to 48° and is free of singularity throughout the overall workspace. In addition, a set of machining test of S-shaped workpiece is implemented to demonstrate the 5-axis machining capability of the prototype.
4) Our further investigations will be focused on the issues of dimensional optimization, structure enhancement, precision design as well as cutting parameters optimization of the proposed hybrid machine tool.

Funding

This work is supported by the Open Fund of the State Key Laboratory for Mechanical Transmissions, Chongqing University (Grant no. SKLMT-ZDKFKT-202003), the Industry-Academy Cooperation Project of Fujian Province (Grant no. 2019H6006) and the Natural Science Foundation for Distinguished Young Scholar of Fujian Province (Grant no. 2020J06010). The corresponding author is also thankful to the sponsor of National Natural Science Foundation of China (Grant no. 51875105).

Declaration of conflicting interests

The author(s) declared no potential conflicts of interest with respect to the research, authorship, and/or publication of this article.

References

[1] L. Uriarte, M. Zatarain, D. Axinte, et al., Machine tools for large parts. CIRP Annals-Manufacturing Technology, 2013, vol.62, no.2, pp.731-750. DOI: https://doi.org/10.1016/j.cirp.2013.05.009

[2] C. L. Dong, H.T. Liu, J.L. Xiao, et al., Dynamic modeling and design of a 5-DOF hybrid robot for machining. Mechanism and Machine Theory, 2021, vol.165, pp.104438. DOI: https://doi.org/10.1016/j.mechmachtheory.2021.104438

[3] Y. Liu, M. Wan. W. Xing, et al., Identification of position independent geometric errors of rotary axes for five-axis machine tools with structural restrictions. Robotics and Computer-Integrated Manufacturing, 2018, vol.53, pp.45-57. DOI: https://doi.org/ 10.1016/j.rcim.2018.03.010

[4] F. E. Marcelo, L. E. Luis, P. Hilde, et al., Analysis of a single-edge micro cutting process in a hybrid parallel-serial machine tool. International Journal of Mechanical Sciences, 2018, vol.151, pp.222-235. DOI: https://doi.org/10.1016/j.ijmecsci.2018.11.023

[5] C. L. Dong, H. T. Liu, W. Yue, et al., Stiffness modeling and analysis of a novel 5-DOF hybrid robot. Mechanism and Machine Theory, 2018, vol.125, pp. 80-93. DOI: https://doi.org/10.1016/j.mechmachtheory.2017.12.009

[6] S. Lu, Y. M. Li, B. X. Ding, Kinematics and dynamics analysis of the 3PUS-PRU parallel mechanism module designed for a novel 6-DOF gantry hybrid machine tool. Journal of Mechanical Science and Technology, 2020, vol.34, no.1, pp.345-357. DOI: https://doi.org/10.1007/s12206-019-1234-9

[7] B. Hu, Y. Shi, L. Xu, et al., Reconsideration of terminal constraint/mobility and kinematics of 5-DOF hybrid manipulators formed by one 2R1T PM and one RR SM. Mechanism and Machine Theory, 2020, vol.149, pp.103837. DOI: 10.1016/J.MECHMACHTHEORY.2020.103837

[8] X. Q. Tang, X. M. Chai, L. W. Tang, et al., Accuracy synthesis of a multi-level hybrid positioning mechanism for the feed support system in FAST. Robotics and Computer-Integrated Manufacturing, 2014, vol.30, pp. 565-575. DOI: https://doi.org/10.1016/j.rcim.2014.03.002

[9] Y. Y. Song, J. Wu, G. Yu, et al., Dynamic characteristic prediction of a 5-DOF hybrid machine tool by using scale model considering the geometric distortion of bearings. Mechanism and Machine Theory, 2020, vol.145, pp.103679. DOI: https://doi.org/10.1016/j.mechmachtheory.2019.103679

[10] M .Weck, D. Staimer, Parallel kinematic machine tools-current state and future potentials. CIRP Annals-Manufacturing Technology, 2002, vol.51, no.2, pp.671-683. DOI: https://doi.org/10.1016/S0007-8506(07)61706-5

[11] D. R. Miguel, V. Angel, et al., Model-based control of a 3-DOF parallel robot based on identified relevant parameters. IEEE/ASME Transactions on Mechatronics, 2013, vol.18, no.6, pp.1737-1744. DOI: https://doi.org/10.1109/TMECH.2012.2212716

[12] A. Ruiz, F. J. Campa, et al., Experimental validation of the kinematic design of 3-PRS compliant parallel mechanisms. Mechatronics, 2016, vol.39, pp.77-88. DOI: https://doi.org/10.1016/j.mechatronics.2016.08.006

[13] L. O. Jose, W. Scott, New PKM Tricept T9000 and its application to flexible manufacturing at aerospace industry. SAE International, Los Angeles, USA, 2007, Paper No. 07ATC-94.

[14] K. Neumann, The key to aerospace automation. aerospace manufacturing and automated fastening conference and exhibition. Detroit, USA, 2006, Paper No. 2006-01-3144.

[15] P. C. López-Custodio, R. Fu, J. S. Dai, et al., Compliance model of Exechon manipulators with an offset wrist. Mechanism and Machine Theory, 2021, vol.167, pp.104558. DOI: https://doi.org/10.1016/j.mechmachtheory.2021.104558

[16] D. Zhang C. Gosselin, Kinetostatic analysis and design optimization of the tricept machine tool family. Journal of Manufacturing Science and Engineering, 2002, 124(3):725-733, Paper No. A7-282. DOI: https://doi.org/10.1115/1.1471529

[17] H. Shin, S. Lee, J. Jeong, et al., Antagonistic stiffness optimization of redundantly actuated parallel manipulators in a predefined workspace. IEEE/ASME Transactions on Mechatronics, 2013, vol.18, vol.3, pp.1161-1169. DOI: https://doi.org/10.1109/TMECH.2012.2198224

[18] T. Sun, X. M. Huo, Type synthesis of 1T2R parallel mechanisms with parasitic motions. Mechanism and Machine Theory, 2018, vol.128, pp. 412-428. DOI: https:// doi.org/10.1016/j.mechmachtheory.2018.05.014.

[19] G. Gogu, Structural Synthesis of Fully-Isotropic Translational Parallel Robots via Theory of Linear Transformations. Eur. J. Mech. A. Solids, 2014, vol.23, no.6, pp. 1021–1039. DOI: https://doi.org/10.1016/J.EUROMECHSOL.2004.08.006

[20] X. Y. Liu, Q. Yang, et al., Design, modeling and analysis of a novel self-crossing mechanism. Mechanism and Machine Theory, 2021, vol.162, pp. 104358. DOI: https://doi.org/10.1016/j.mechmachtheory.2021.104358.

[21] J. Wei, J. S. Dai, Reconfiguration-Aimed and Manifold-Operation Based Type Synthesis of Metamorphic Parallel Mechanisms with Motion between 1R2T and 2R1T. Mech. Mach. Theory, 2019, vol.139, pp. 66–80. DOI: https://doi.org/10.1016/j.mechmachtheory.2019.04.001

[22] S. F. Yang, T. Sun, et al., A finite screw approach to type synthesis of three-DOF translational parallel mechanisms. Mechanism and Machine Theory, 2016, vol.104, pp. 405-419. DOI: https:// doi.org/10.1016/j.mechmachtheory.2016.02.018.

[23] Q. Li, J. Hervé, 1T2R Parallel Mechanisms without Parasitic Motion. IEEE Trans. Robot., 2010, vol.26, no.3, pp. 401–410. DOI: https://doi.org/10.1109/TRO.2010.2047528

[24] S. Yang , T. Sun , T. Huang, Type synthesis of parallel mechanisms having 3T1R motion with variable rotational axis. Mechanism and Machine Theory, 2017, vol.109, pp. 220-230. DOI: https:// doi.org/10.1016/j.mechmachtheory.2016.11.005.

[25] H. L. Fang, T. F. Tang, J. Zhang, Kinematic analysis and comparison of a 2R1T redundantly actuated parallel manipulator and its non-redundantly actuated forms. Mechanism and Machine Theory, 2019, vol.142, pp.103587. DOI: https://doi.org/10.1016/j.mechmachtheory.2019.103587

[26] J. A. Saglia, J. S. Dai, D. G. Caldwell, Geometry and kinematic analysis of a redundantly actuated parallel mechanism that eliminates singularities and improves dexterity. Journal of Mechanical Design, Transactions of the ASME, 2008, vol.130, no.12, pp.1245011-1245015. DOI: https://doi.org/10.1115/1.2988472

[27] M. Luces, J. Mills, B. Benhabib, A review of redundant parallel kinematic mechanisms. Journal of Intelligent and Robotic Systems, 2017, vol.86, no.2, pp.175-198. DOI: https://doi.org/10.1007/s10846-016-0430-4

[28] J. Kim, F. Park, S. Ryu, et al., Design and analysis of a redundantly actuated parallel mechanism for rapid machining. IEEE Transactions on Robotics and Automation, 2001, vol.17, no.4, pp.423–434. DOI: https://doi.org/10.1109/70.954755
[29] D. Wang, R. Fan, M. Y. Chen, Performance enhancement of a three-degree-of-freedom parallel tool head via actuation redundancy. Mechanism and Machine Theory, 2014, vol.71, pp.142–162. DOI: https://doi.org/10.1016/j.mechmachtheory.2013.09.006
[30] F. G. Xie, X. Liu, Y. H. Zhou, Optimization of a redundantly actuated parallel kinematic mechanism for a 5-degree-of-freedom hybrid machine tool. Proceedings of the Institution of Mechanical Engineers Part B Journal of Engineering Manufacture, 2014, vol.228, no.12, pp.1630-1641. DOI: https://doi.org/10.1177/0954405414522450
[31] H. T. Liu, T. Huang, A. Kecskemethy, et al., Force/motion transmissibility analyses of redundantly actuated and overconstrained parallel manipulators. Mechanism and Machine Theory, 2017, vol.109, pp.126-138. DOI: https://doi.org/10.1016/j.mechmachtheory.2016.11.011
[32] T. F. Tang, H. L. Fang, J. Zhang, Hierarchical design, laboratory prototype fabrication and machining tests of a novel 5-axis hybrid serial-parallel kinematic machine tool. Robotics and Computer-Integrated Manufacturing, 2020, vol.64, pp.101944. DOI: https://doi.org/10.1016/j.rcim.2020.101944
[33] S. J. Jiang, C. C. Chi, H. L. Fang, et al., A minimal-error-model based two-step kinematic calibration methodology for redundantly actuated parallel manipulators: an application to a 3-DOF spindle head. Mechanism and Machine Theory, 2021, vol.167: 104532. DOI: https://doi.org/10.1016/j.mechmachtheory.2021.104532
[34] Q. C. Li, N. B. Zhang, F. B. Wang, New indices for optimal design of redundantly actuated parallel manipulators. Journal of Mechanisms and Robotics, 2017, vol.9, no.1: 011007. DOI: https://doi.org/10.1115/1.4035126
[35] X. Chai, Q. C. Li, W. Ye, Mobility analysis of overconstrained parallel mechanism using Grassmann-Cayley algebra. Applied Mathematical Modelling, 2017, vol.51, pp.643-654. DOI: https://doi.org/10.1016/j.apm.2017.07.044
[36] Q. C. Li, L. M. Xu, C. Yang, et al., Elastostatic stiffness modeling of overconstrained parallel manipulators. Mechanism and Machine Theory, 2018, vol.122, pp.58-74. DOI: https://doi.org/10.1016/j.mechmachtheory.2017.12.011
[37] F. C. Li, Q. Zeng, F. E. Kornel, et al., A calibration method for overconstrained spatial translational parallel manipulators. Robotics and Computer-Integrated Manufacturing, 2019, vol.57, pp. 241-254. DOI: https:// doi.org/10.1016/j.rcim.2018.12.002
[38] A. Muller, Consequences of geometric imperfections for the control of redundantly actuated parallel manipulators. 2010, vol.26, no.1, pp. 21-31. DOI: https:// doi.org/ 10.1109/TRO.2009.2035742
[39] Z. Huang, Q. C. Li, et al., Theory of parallel mechanism. Springer Netherlands, 2013.
[40] C. Y. Ying, M. H. Yen, et al., Non-spherical ball-socket joint design for Delta-type robots. Mechatronics, 2017, vol.45, pp. 14-24. DOI: https:// doi.org/ 10.1016/j.mechatronics.2017.05.003.
[41] S. Han, S. Ge, Effect of femoral head shape on mechanical behaviors of artificial hip joint. International conference on biomedical engineering and informatics, 2010.
[42] F. C. Wang, Z. M. Jin, Effect of on-spherical bearing geometry on transient elastohydrodynamic lubrication in metal-on-metal hip joint implants. ARCHIVE Proceedings of the Institution of Mechanical Engineers Part J Journal of Engineering Tribology, 2007, vol.221, pp. 379-389. DOI: https:// doi.org/ 10.1243/13506501JET249.
[43] R.S. Ball, Treatise on the Theory of Screws. Cambridge University Press, New York, 1900, Reprint 1998.
[44] C. Qiu, J. S. Dai, An Introduction to Screw Theory. In: Analysis and Synthesis of Compliant Parallel Mechanisms-Screw Theory Approach. Springer Tracts in Advanced Robotics, 2021, vol.139, pp.17-31. DOI: https://doi.org/10.1007/978-3-030-48313-5
[45] Q. C. Li, L.M. Li, et al., New Family of RPR-Equivalent Parallel Mechanisms: Design and Application. Chinese Journal of Mechanical Engineering, 2017, vol.30, no.2, pp.11-15. DOI: https: //doi.org/ 10.1007/s10033-017-0045-0
[46] E. O. Teuţan, A. Oarcea, et al., Shape optimization for the inscribed workspace of a prismatic actuated 2PRR parallel robot. 2021, The 9th International Conference on Modern Power Systems (MPS), pp. 1-6, DOI: //doi.org/ 10.1109/MPS52805.2021.9492540.
[47] X. Li, D. Zlatanov, M. Zoppi, et al., Stiffness estimation and experiments for the exechon parallel self-reconfiguring fixture mechanism. ASME 2012 International Design Engineering Technical Conferences and Computers and Information in Engineering Conference, Volume 4: 36th Mechanisms and Robotics Conference, Parts A and B, Chicago, USA, 2012. DOI: https://doi.org/10.1115/DETC2012-70993
[48] Y. D. Xu, D. S. Zhang, et al., Type synthesis of the 2R1T parallel mechanism with two continuous rotational axes and study on the principle of its motion decoupling. Mechanism and Machine Theory, 2017, vol. 108, pp. 27-40. DOI: https:// doi.org/ 10.1016/j.mechmachtheory.2016.09.007.